



UNIVERSIDAD CARLOS III DE MADRID

BACHELOR THESIS

AEROSPACE ENGINEERING

Experimental Setup for PIV

Author: Matías Ayrton Pérez Cagegi

Tutors: Stefano Discetti and Marco Raiola

25/09/2018

Acknowledgements

To my family, who always backed me up no matter what, and helped me more than I can still realize. To my friends back at home, who make me who I am today, and always forced me out of home during exams.

To the amazing friends I met at university. All of you have showed me how many different ways of thinking there can be, and helped me to grow as a person and enjoy more meeting new people.

To Stefano Discetti, who cared for this project sometimes more than anyone, and provided wise advice, infinite patience and the good vibes necessary to make a project like this very enjoyable. To Marco Raiola, for showing me how important are details down in the laboratory. To Carlos Cobos, for carrying out all jobs we dropped on him and more, and always having a good smile when working or when the times were rough.

Abstract

Turbulent flows have a number of interesting characteristics such as their mass and heat transfer. One which is very important in the field of aeronautics, is the role played by turbulence in aerodynamic noise production. In fact, one of the main sources of noise within an aircraft engine is the one coming from the exhaust jet (Called "Jet noise"). This comes into conflict with the airport regulations that intend to reduce noise in favour of the surrounding populations, making the study of turbulences with the aim of jet noise reduction an interesting idea.

In this project, a facility within the university was created, in order to be able to reproduce what is called a free jet, a flow similar to the one found in an engine exhaust. Then, the resulting jet, which had a Mach number of 0.084 and a Reynolds number of $19 \cdot 10^3$ was tested in the laboratory. The procurement, design and assembly of all the elements of the facility has been documented here.

In order to validate the facility, and check that the flow obtained with the facility actually resembled that of an engine outlet, the velocity fields, as well as the turbulent intensities, were measured using a technique called Particle Image Velocimetry (PIV). The results were post-processed and checked with the literature, being one important validation condition the fact that the flow had to achieve what is known as self-similarity. This condition should be ideally reached after a specific distance downstream from the nozzle exit.

This axial distance is usually measured in diameters, and this experiment covered up to 25 diameters, approximately. In this first approach, the self-similarity was not directly looked for, but rather, evidence that it was attainable with this facility were aimed for.

The comparison was made, and the results indicated that the self-similarity was not clearly attained in this experiment, but they suggested that it could be observed by extending the field of analysis a few more axial distances.

Contents

| | |
|---|-------------|
| Abstract | iii |
| List of Figures | ix |
| List of Tables | xiii |
| 1 Introduction | 1 |
| 1.1 Aeroacoustics: Socio-economical framework | 2 |
| 1.2 State of the art | 4 |
| 1.2.1 The free round jet | 4 |
| 1.2.2 Self-similarity in turbulent jets | 7 |
| 1.2.3 Jet noise | 7 |
| 1.3 Objectives and project Outline | 8 |
| 2 Design and manufacturing of the experimental setup | 11 |
| 2.1 Overview of the final assembly | 11 |
| 2.2 The mixing chamber | 14 |
| 2.3 The second chamber | 17 |

| | | |
|----------|--|-----------|
| 2.4 | The stagnation chamber | 22 |
| 2.5 | The nozzle | 25 |
| 2.5.1 | The 3D printing | 31 |
| 2.6 | The supporting frame | 34 |
| 3 | Experimental procedure | 39 |
| 3.1 | Operating principles of PIV | 39 |
| 3.2 | Instrumentation | 42 |
| 3.2.1 | Temperature and pressure sensors | 42 |
| 3.2.2 | The laser | 42 |
| 3.2.3 | The camera | 43 |
| 3.3 | Data measurements | 44 |
| 3.4 | Data treatment | 47 |
| 4 | Results analysis and comparison with literature | 49 |
| 5 | Temporal distribution of the project | 59 |
| 6 | Costs calculation | 61 |
| 7 | Regulatory frame and future possibilities | 63 |
| 7.1 | Laboratory safety rules | 63 |
| 7.2 | Noise legislations | 63 |
| 7.3 | Improvements | 64 |

| | |
|----------------------|----|
| 8 Project conclusion | 65 |
| Bibliography | 67 |

List of Figures

| | | |
|-----|--|----|
| 1.1 | Aircraft noise reduction through the years. Extracted from [22]. | 3 |
| 1.2 | Two different pictures of free jets. In the left [32], the toroidal vortices can be better appreciated. In the right [40], the general structure is much more clear. | 5 |
| 1.3 | Radial velocity profiles at different axial distances. Extracted from [31]. | 6 |
| 1.4 | Insight over the different types of noise sources of an aircraft. Extracted from [20] | 8 |
| 2.1 | Full setup already assembled. The labels indicate the visible elements names. | 12 |
| 2.2 | Schematic of the setup, as seen from above. The stagnation chamber cannot be seen here, as it is below the nozzle, and the red dot shows the point of view of figure 2.1 | 13 |
| 2.3 | Mixing chamber. The light grey connections between the central cross and the ends are the glued PVC tubes. | 15 |
| 2.4 | Commercial image of the valve, obtained from the supplier's webpage . . | 16 |
| 2.5 | Laskin nozzle. | 17 |
| 2.6 | Second PVC cross. The blue arrows indicate the flow direction after being assembled in the setup. | 18 |
| 2.7 | Top view of the machined sleeved flange. | 19 |

| | | |
|------|--|----|
| 2.8 | Complete impinging plate. | 19 |
| 2.9 | Machined lid of the impinging plate. | 19 |
| 2.10 | Drawing of the machined lid. | 19 |
| 2.11 | Miller used to drill the impinging plate. | 20 |
| 2.12 | Angle variator that goes attached to the miller. | 20 |
| 2.13 | Top view of a sleeved flange. | 20 |
| 2.14 | Bottom view of a sleeved flange. | 20 |
| 2.15 | Bottom view of a blind flange. | 21 |
| 2.16 | Top view of a blind flange. | 21 |
| 2.17 | Top view of the machined blind flange. | 21 |
| 2.18 | Bottom view of the machined blind flange. | 21 |
| 2.19 | Mosquito net. | 23 |
| 2.20 | Mosquito net already mounted within the frames. | 24 |
| 2.21 | Two different views of the printed honeycomb. | 25 |
| 2.22 | Nomenclature followed, extracted from [28]. | 28 |
| 2.23 | Wall shape function. | 30 |
| 2.24 | Wall shape derivative behaviour. | 31 |
| 2.25 | Top view of the printed nozzle | 32 |
| 2.26 | Bottom view of the printed nozzle | 32 |
| 2.27 | Side view of the printed nozzle. | 33 |

| | | |
|------|---|----|
| 2.28 | Close-up of the wall shape. The deformed part can be appreciated here, at the left-most of the nozzle wall. | 33 |
| 2.29 | Close view of the interior of the nozzle. The wrinkled surface can be appreciated here, which remained even after the polishing with acetone. | 34 |
| 2.30 | Empty mounted structure. | 35 |
| 2.31 | Setup with the nozzle mounted in the structure. | 35 |
| 2.32 | One of the sides of the profiles. | 36 |
| 2.33 | Front view of the profile. | 36 |
| 2.34 | One of the brackets used for the profiles. | 36 |
| 2.35 | Mounted set of brackets and profiles. | 37 |
| 2.36 | One of the feet of the structure. | 37 |
| 2.37 | Blanket mounted in the structure. | 38 |
| 3.1 | Typical PIV setup for a single-camera data measurement. Extracted from [40]. | 41 |
| 3.2 | Calibration target for the camera. | 44 |
| 3.3 | Close-up of the target. | 44 |
| 3.4 | Schematic of the field of vision of each of the pictures taken, along with the reference axis. | 47 |
| 4.1 | Contour of the axial velocity field | 50 |
| 4.2 | Contour of the radial velocity field | 50 |
| 4.3 | Contour and radial profile of u^2 | 52 |
| 4.4 | Contour and radial profile of v^2 . Some values of the contour are missing for the sake of a more clear colouring of the image. | 52 |

| | | |
|------|--|----|
| 4.5 | Contour and radial profile of uv . Some values (The highest positives, which go up to 0.15) of the contour are missing for the sake of a more clear colouring of the image. | 53 |
| 4.6 | Radial profiles of Reynolds stresses as in Pope's book. | 54 |
| 4.7 | Radial profiles of the mean axial velocity. | 55 |
| 4.8 | Mean axial velocity against radial distance | 56 |
| 4.9 | Variation of half-radius with axial distance. One of the slope values from Pope [31] is also plotted to compare. Since it is not specified in the book, x_0 is set to 0. | 57 |
| 4.10 | Variation of mean velocity with axial distance. One of the B values from Pope is also plotted to compare. | 58 |
| 5.1 | Gantt chart of the full project. In green, the theoretical work is presented. The work of procurement and design of the structure is marked with blue tones. The assembly of the structure is painted in brown colours. 60 | |

List of Tables

| | | |
|-----|--|----|
| 2.1 | Characteristics of the nozzle | 27 |
| 2.2 | Coefficients defining the nozzle wall shape. | 29 |
| 3.1 | Laser characteristics. | 43 |
| 3.2 | Camera characteristics. | 43 |
| 3.3 | Data in Run 1 | 45 |
| 3.4 | Data in Run 2 | 45 |
| 3.5 | Data in Run 3 | 46 |
| 3.6 | Data in Run 4 | 46 |
| 3.7 | Data in Run 5 | 46 |
| 6.1 | Project costs. | 61 |

Chapter 1

Introduction

Up to these days, turbulence is one of the biggest unknowns in the field of fluid mechanics. Despite it being easily spotted in our daily life like when mixing the sugar in the coffee or feeling how the air gets into a car with its open window, making quantitative measures of its behaviour is far more difficult. One of the problems is that, in general, one cannot see what happens inside the fluid, unless some other element (be it a solid or another fluid) is there to give a hint of what the medium of interest is doing. The main problem arises with the fact that the turbulence behaviour is tridimensional, chaotic, and there are a number of different vortical structures which sometimes have different characteristics, making its study a very difficult task.

However, why would understanding turbulent phenomena be so important? Because, it presents very different conditions with respect to laminar flows. These differences have a wide variety of industrial applications, and in the field of aeronautics, the study of turbulence has very interesting applications related with noise reduction in aircraft.

Appart from the noise problems, turbulent flows present some interesting characteristics, as due to the increased particle mixing, they have an increased mass and heat transfer with respect to laminar flows.

This began to be implemented for turbine blade cooling, where it showed better results than convective cooling ([4], [27]). It has been also used by the food industry, in ovens ([37]) and in a variety of food cooking in processes that go from baking to drying or freezing ([34]). Liquid jets have also some applications, as ([10]) explain, like cooling microprocessors and other small electronic devices.

Lastly, the study of mixing is very helpful for combustion enhancement, which could potentially reduce the length of afterburners in aircraft engines.

However, as already mentioned, in the field of aeronautics what is interesting is the noise reduction. Thus, the objective of the project is to design, procure and assembly a jet facility that allows the study of free jets, as they constitute an important part of the noise generated by aircraft engines.

It could be said that the study of the noise sources related to turbulence began to gain presence in 1952, when James Lighthill released his paper *On sound generated aerodynamically, Part 1: general theory* [26]. This gave birth to the so-called field of aeroacoustics, in which the objective was to find a connection between the turbulent phenomena inside a flow and the noise it generates, for which Lighthill formulated what is today known as "Lighthill's aeroacoustic analogy".

Even if some revisions have been done on his equations [16], the field still poses a great challenge to scientists and engineers, and has still a lot of potential applications.

1.1 Aeroacoustics: Socio-economical framework

Since the noise issues started to be investigated not long ago, in terms of the development of a technology, nowadays it is still a hot topic in the field of aeronautics. Even though more and more silent aircraft are being launched to the market, the regulations constantly becoming tighter make up for a challenge for the technology. The main reason behind these regulations is the problems that noise cause on the population's health ([7]).

Morrell et al. reviewed a number of studies regarding this aspect [29]. There is still some controversy regarding some of these studies, due to the large amount of variables that can influence the health risks accounted for, but some conclusions can still be drawn. The exposure of noise introduces some level of annoyance into the population, which is more acute when the noise is on the form of intensity peaks, rather than a lower but averaged noise. Tarnopolsky was one of the first ones that dug into this matter, noticing that there were population groups that were susceptible to noise and had increased risk of suffering a number of health issues due to this. [38].

Also, long-term exposure is generally accepted to increase stress levels, which is detrimental to body and mental health. The mechanisms for this stress level to arise include the aforementioned annoyance, as well as sleep disruption. Eriksson et al. indicated that a long term exposure of 10 years increased the risk of suffering from heart diseases, although this correlation is higher in groups with an already higher risk the mean population, like smokers or elder people [9].

The reason to choose this specific date is because Huff considered this to be "stage 3" on aircraft noise reduction [22]. This stage is used as a reference in Fig. 1.1 to acknowledge the reduction in Effective Perceived Noise Level (EPNL, also called EPN in dB in the picture).

Figure 1.1: Aircraft noise reduction through the years. Extracted from [22].

Silent aircraft would not only directly mitigate these medical issues, but would also allow for complete night operations of commercial flights, further increasing the economic benefits of the aeronautical industry. This is so much beneficial that initiatives are being held in Europe in order to promote new ideas to reduce noise issues. Two examples of programmes are the Horizon 2020 ([18],[17]) and the Clean Sky, the latter being more specifically focused on the noise.

The green regional aircraft that are being developed under this latter project can presumably reduce the perceived noise by the population surrounding an airport in 50% by the year 2020[21]. This shows the potential that this field of study has.

1.2 State of the art

1.2.1 The free round jet

The free jet not only resembles the exit nozzle flow of a turbofan, but it also can be taken as an elementary flow, in which the different coherent structures can be appreciated with little perturbations. Coherent structures are the macroscale turbulent structures that, disregarding variations due to fluctuations of vorticity, present certain continuity of this magnitude. Examples are the ring vortices that were explained later in this section.

Being able to observe more clean coherent structures allows to isolate them and study them separately. This may allow, in the very end, to tackle the most noisy structures specifically, or to design different solutions for the different noise sources present in the jet. Breaking down the problem like this is a common practice in engineering, and this project's intention is to help the university doing this with the field of turbulent flows.

The free jet is a stream of air coming out from a nozzle and going into the free ambient. That is, it does not have any surface to collide with, differing at this point from impinging jets. Jets can also be submerged or non-submerged, depending on the medium into which they discharge. If the medium is the same as the jet, it is a submerged jet, and it will be the one treated here. In order to furtherly clean the structures of the jet, this surrounding air must be stagnant.

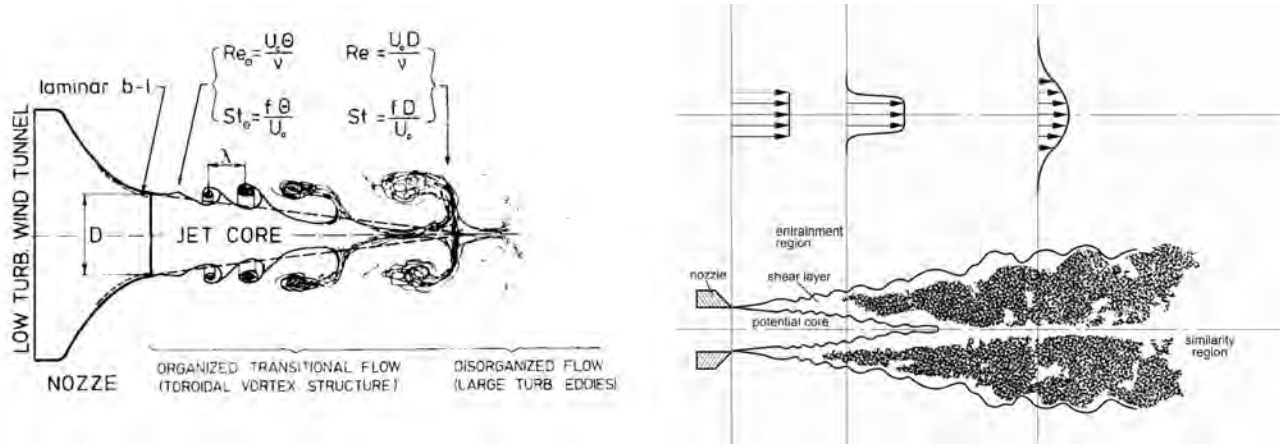


Figure 1.2: Two different pictures of free jets. In the left [32], the toroidal vortices can be better appreciated. In the right [40], the general structure is much more clear.

Figures 1.2 a (Left) and b (Right) show two schematics of the different parts of a free jet. In Fig. 1.2 b the general structure can be observed, with the ideal velocity profiles put on top of these areas.

The central region near the nozzle is called the potential core. Here, the flow has zero vorticity, and the velocity is equal to the one that left the nozzle. This is because it is still unperturbed, and thus the flow remains as it was when leaving the nozzle.

The air that comes out of the nozzle has more momentum than the ambient air, and, in the outer-most part of the jet, where it comes in contact with the ambient, a friction force is developed due to the velocity gradient. The air that flows faster is directed outwards from the jet axis, creating some vortices. These vortices, called entrainment vortices and seen better in Fig. 1.2 a, are responsible of the stagnant air going into the jet, breaking up the shear layer. In the 3D space, they develop around the jet, being sometimes called ring vortices.

Some authors like Poppiel and Trass argue that these vortices are responsible of some kind of pulsating variation in the pressure at the nozzle exit, producing a synchronization in the appearance of new ring vortices [32]. This is one of the reasons that motivates the use of a uniform velocity profile for round jet studies.

Upon breaking, the shear layer erodes progressively the potential core introducing momentum in it and attracting the flow outside, producing each time bigger vortices around the jet. The potential core disappears usually at approximately 6.5 diameters ([40], [14], [27]).

After some time, these vortices become unstable, and break or pair with each other. It is believed these mechanisms, along with some others, are important noise sources. Hussain [24] explains vortex pairing with what he calls cut-and-connect mechanisms, and gives more insight on why vortex pairing produces noise.

When the potential core disappears, the jet keeps decaying and spreading, as the effect of the external shear layer keeps influencing the jet. Decaying means that the maximum value of the radial profile of the mean axial velocity is lower. Spreading refers to the fact that this profile becomes flatter. Even though this effects can be seen in Fig. 1.2 b, it can be better appreciated in Fig. 1.3.

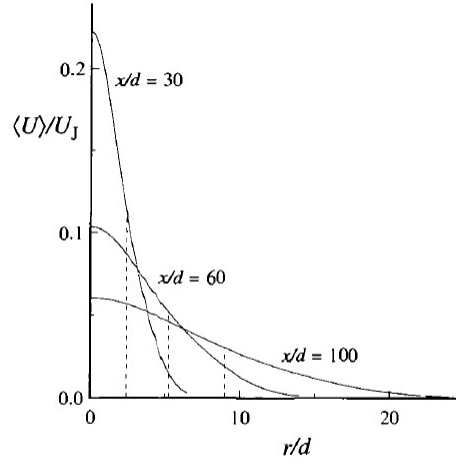


Fig. 5.2. Radial profiles of mean axial velocity in a turbulent round jet, $Re = 95,500$. The dashed lines indicate the half-width, $r_{1/2}(x)$, of the profiles. (Adapted from the data of Hussein *et al.* (1994).)

Figure 1.3: Radial velocity profiles at different axial distances. Extracted from [31].

In this figure, $\langle U \rangle / U_J$ is the dimensionless mean velocity radial profile (That is, a 2D plane of the velocity profile), of only one of the axisymmetric sides of the jet. U is used for the axial velocity of the jet, while U_J is the bulk velocity. The angular brackets, " $\langle \rangle$ " indicate the time average of the magnitude they are surrounding.

r/d is the radial distance from the jet center, r , divided by the exit diameter of the nozzle, d , whereas x/d indicates the axial distance from the jet exit. Again, d is the diameter of the nozzle, and x is the distance.

1.2.2 Self-similarity in turbulent jets

One of the most important features of the free jet is that, after a certain distance, the jet becomes self-similar. This means that its dimensionless velocity profile, plotted against the dimensionless radial distance follows the same behaviour, regardless of the axial distance.

There is some controversy regarding the point at which this happens. The main theory source for this project, Pope [31], settles $x/d > 30$, and while other authors ([14], [6] or [12]) usually agree on full self-preservation at $x/d > 40$, there are experiments that result in self-preservation after $x/d > 65$ ([15]).

Furthermore, different magnitudes of the flow may reach self-similarity at different distances. Boersma [3] points out that: *"the mean velocity profile and the turbulent shear stress profile become self-similar beyond a downstream distance of about 10 orifice diameters. For other statistics such as the turbulent velocity fluctuations self-similarity is expected only after about 35 diameters"*. In order to obtain the maximum data to contrast, the distance to study will be the maximum that can be reached within the laboratory of the university.

The self-similarity condition of the flow is of maximum interest as it allows to apply the results of a single experiment to different conditions, and hence it will be one of the main objectives to achieve with the facility. Some authors ([11], [25]) argue that the self-similarity of the flow has some dependency on the initial conditions, but since the present paper is a first approach for this kind of investigations in the university, that topic will not be tackled here.

1.2.3 Jet noise

It has been mentioned that the turbulent jet that emerges from the exit nozzle of a jet is a source of noise, but how important is it, compared to how much noise an engine can produce? At a first glance, the rotors could be regarded as more noisy, but in figure 1.4, it can be observed how both the jet exhausts of the turbojet and the fan flows of a commercial aircraft turbofan have a significant importance on the total noise made by an aircraft.

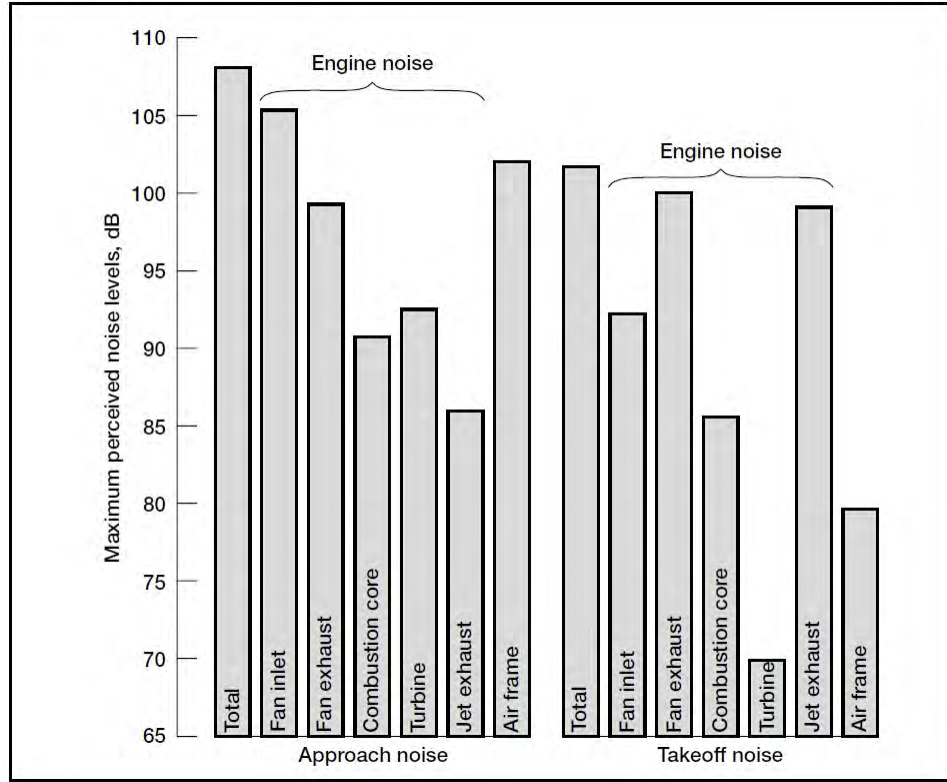


Figure 1.4: Insight over the different types of noise sources of an aircraft. Extracted from [20]

The fan exhaust can reach nearly 100 decibels, which is much more than what is recommended for the health of the population, as stated in section 1.1. In view of this, it is clear that this field has applications that are of use for the society, even though more research is needed in the field of aircraft noise (As the exhaust does not comprehend the full extent of aircraft noise).

1.3 Objectives and project Outline

The final objective of this project is to design and manufacture a jet facility within the university laboratory. This setup will allow the use of Particle Image Velocimetry (PIV, explained in section 3.1) to study free jets under different conditions. The structure's correct functioning will be validated by comparing the results of the turbulent magnitudes obtained with the available literature. For this, a number of figures will be compared to those of the available literature, mainly [31].

In Chapter 2, the complete setup implemented and used to take PIV measurements will be explained. The contribution of the author was mostly focused in this part. It consisted on searching the different pieces that were needed and procuring them, designing any piece that was not going to be directly bought and needed to be 3D-printed and defining the plans for machining the pieces. Lastly, the author collaborated with the assembly of the facility.

First, an overview of the final result is shown, and all elements are explained slightly, in order to give a general idea. Then, a section for each element will give the necessary in-depth.

Chapter 3 begins with an explanation of the technique used to obtain the measurements, the PIV. It also goes over the different instrumentation needed to carry out the tests, and explains the post-processing applied to the data.

In chapter 4, the validation of the structure is carried out. Different magnitudes obtained with the experiments are compared with the results from literature, and conclusions on them are extracted.

Chapters 5 and 6 contain an overview of how the project was organized in time, and how much money it has cost to carry it out.

Chapter 2

Design and manufacturing of the experimental setup

2.1 Overview of the final assembly

Fig. 2.1 showcases the final result of the project. The main supporting frame, formed by grey aluminum profiles, can be seen with a blanket covering it, and in the middle, the nozzle and the stagnation chamber, the PVC tube which is right on top of the cross that is on the floor. Consider, however, that there are elements not visible in the picture, and images of them will be shown in their corresponding sections.

These elements can be further seen in fig. 2.2, where a schematic is presented, seen from above. The red point indicates the place from which the picture in fig. 2.1 was taken. The hoses that connect the flow from the pressure lines are indicated with straight blue lines, with an arrow that points the direction of the flow. The rest of items are labeled either inside the boxes representing their location, or connected with their label by a black line.

Lastly, notice that the stagnation chamber is not in the schematic because it is under the nozzle and that most of the boxes do not represent the real relative size of the elements, but rather were sized to fit the labels and organize the image.

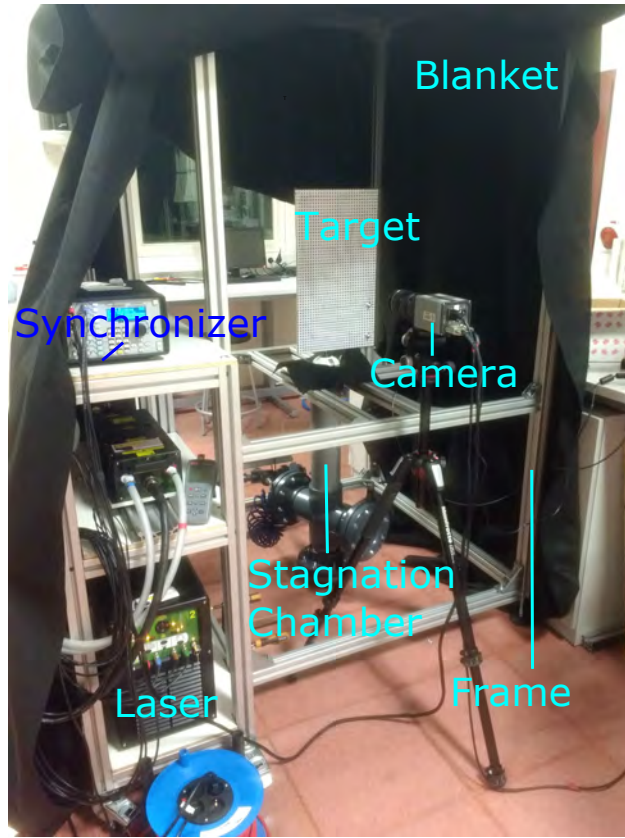


Figure 2.1: Full setup already assembled. The labels indicate the visible elements names.

The flow of air comes out from a pressure line installed in the laboratory. This line has its tanks outside the building, and thus the air comes at ambient temperature, and with a design pressure of at most 3 bars. Since the pressure line can reach up to 6 bars, the head loss in this experiment will be disregarded, as any unexpectedly high drop can be easily compensated by increasing the power delivered to the pressure line. Given the case of an experiment that needs to use more of the power of the pump, making the head losses a problem, a proper optimization of the different elements that introduce head loss (Hoses, wire screens, etc..., explained in the next pages) should be done. For the moment, a qualitatively correct functioning of the setup is the only objective.

Taking this power availability into consideration, the length of the hoses that connect the different elements was selected by the convenience that it could give during the tests.

Due to the laboratory being not dedicated exclusively to this experiment, it is very likely that it is going to be moved at some point, and also the pressure line outlets are located on walls that are in front of each other, so the hoses were chosen 5 meters long to allow the testing at different points of the laboratory, without having too much of a reorganization inside it.

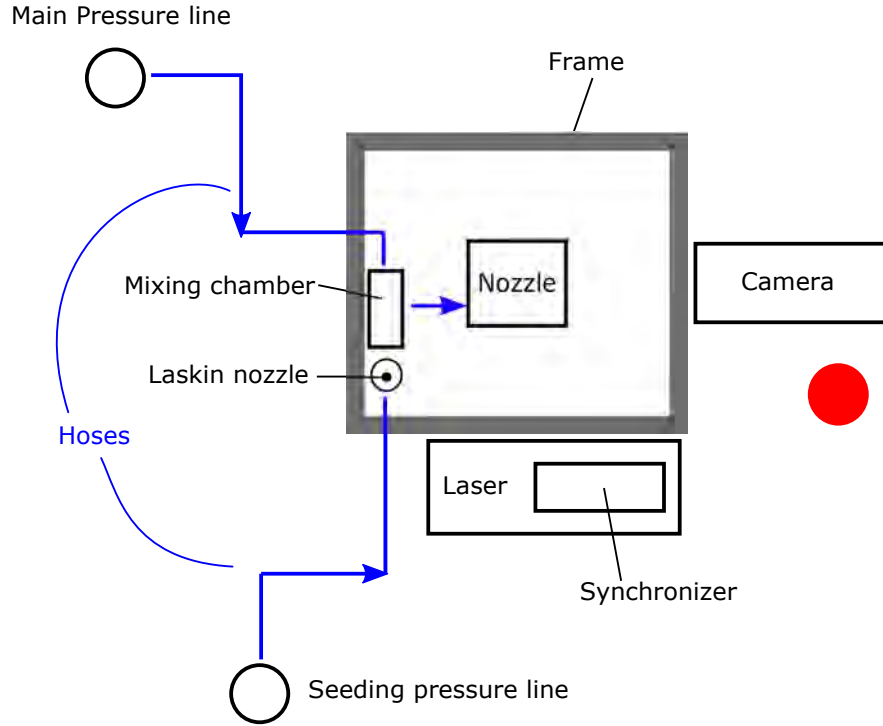


Figure 2.2: Schematic of the setup, as seen from above. The stagnation chamber cannot be seen here, as it is below the nozzle, and the red dot shows the point of view of figure 2.1

The first element that the flow encounters after leaving the pressure line is the so-called mixing chamber (Section 2.2). The purpose of this piece is to control the seeding of scatterer particles that goes into the flow, as well as to achieve a proper mixing. The seeding is introduced thanks to a Laskin nozzle, and the total flow that progresses out of the mixing chamber is controlled by means of a ball valve that allows some already mixed flow to exit the chamber, thus having a control on the seeding instead of just relying on the pressure differences coming from the Laskin nozzle.

The next hose guides the flow into a second, bigger PVC cross (Section 2.3). Here, an impinging plate is located in order to reduce the velocity of the flow before it enters the stagnation chamber. The cross has two exits that are unused at the present moment, as this element is mainly there for its use in future tests.

Hence, in this setup the flow impacts on the impinging plate and goes directly towards the stagnation chamber.

In the stagnation chamber (Section 2.4), the turbulences of the flow are mitigated by means of a honeycomb and a wire screen, making the flow more laminar. At the exit of this element, a convergent nozzle is placed so that the flow is accelerated with a specific velocity profile at the discharge.

The nozzle (Section 2.5) has been designed with 3D design following a specific wall function and then printed in plastic. It is directly attached to the stagnation chamber and the support structure by means of a sleeved flange. Close to the exit of nozzle inlet, a thermocouple and a differential pressure sensor are put in order to measure the total pressure and temperature inside the chamber right before the discharge.

The task of keeping all the setup in place is carried out by a supporting structure (Section 2.6) made from aluminum profiles. It is basically a cage with the shape of a quadrangular prism, with a base of 1 meter and a height of approximately 2.7 meters. This length intends to keep a non-enclosed ambient for the jet, so that it can behave as in a free ambient discharge. This structure is covered by a black blanket made of felt that keeps the seeding particles from filling all the room. It also absorbs a good amount of light, allowing the use of the laser without undesired reflections that could be hazardous, as well as allowing good lighting conditions for the camera to avoid noisy images.

The setup is to be illuminated through the means of a pulsed laser that essentially emits light that is converted into a thin sheet with the use of lenses. With the scattering generated by the seeding, the camera is able to take the adequate images for the post-processing, therefore completing the experimental stage of a PIV measurement (Sections 3.1 and 3.2).

2.2 The mixing chamber

As will be explained in section 3.1, seeding the flow is very important for the PIV technique. This is why the facility requires a mixing chamber (figure 2.3), in order to mix the clean air flow coming from the main pressure line with the seeding coming from the Laskin nozzle.

The core of the mixing chamber is a PVC cross with a nominal diameter of 40 mm and a thickness of 3 mm. Since all the exits are female connections, the male counterparts had to be sealed in order to attach new elements to the cross. These are PVC pipes with 32 and 40 mm of diameter.



Figure 2.3: Mixing chamber. The light grey connections between the central cross and the ends are the glued PVC tubes.

By cutting a small portion of those pipes and sticking them into the cross, the different elements can be linked to the chamber. Two hoses are placed in the chamber, both with the male connector sticking out of this element. The threaded part of each of these ends goes through a hole machined in a 40 mm cap, which is then stuck around the 40 mm PVC pipe segment. This hole has been machined inside the university, and its diameter is slightly smaller than one fourth of an inch (The machine used for it is depicted in 2.11). Applying a bit of pressure, the hose connector can thread the initially smooth inner part of the hole, giving an extra resistance against the pressure applied. Furthermore, it is sealed with silicone to prevent air losses.

The 40 mm cap can be seen already attached around a PVC segment in figure 2.9.

Similarly, the ball valve (figure 2.4) is also attached to the mixing chamber using a previously cut segment of pipe, as it is also made of PVC with a female connector. The valve can be moved manually in non-fixed positions between completely open and fully closed positions, thus allowing a simple control.



Figure 2.4: Commercial image of the valve, obtained from [the supplier's webpage](#).

The last element is the Laskin nozzle (figure 2.5), which provides the seeding to the flow. The working principle of the Laskin nozzle is based on using high pressures to vapourize the fluid. This substance (Called Dy-Ethyl-Hexyl-Sebacate, or DEHS) is in liquid phase and stagnant, separated from the inlet and outlet by an atomizer disk. This disk leaves a very tiny space in which the air can flow, keeping it from leaving too fast and hence increasing pressure to atomize.

Through the disk, a pipe connects the liquid to a second inlet of the pressure line, injecting high pressure air directly into the liquid, vapourizing it in very small droplets that flow upwards and move directly towards the mixing chamber.

Thus, there are two pressure lines going into the facility: The main one, that is providing the majority of the pressure and hence the air mass flow rate, and the secondary one, which simply allows the seeding to go into the chamber and mix with the main stream of air.

Since this Laskin nozzle is used in other facilities such as the wind tunnel of the university, its integration into this system should be non-permanent, and hence using adhesives is discarded. This is why a threaded PVC converter is used in the Laskin nozzle's connector, which is a threaded female with a nominal diameter of 32 mm.

This converter has a smooth female side in which PVC pipes of 32 mm diameter can be glued, allowing it to be glued to the mixing chamber through an adaptor from 32 to 40 mm. This adaptor allows the 32 mm male pipe to match with the 40 mm female cross. Thus, the converter is fixed, while the Laskin nozzle can be unscrewed and easily removed.



Figure 2.5: Laskin nozzle.

2.3 The second chamber

There is an extra PVC cross (Figure 2.6), bearing 110 mm of diameter, placed after the second hose. The objective of the chamber is to allow extra inlets in the facility for, as examples, acoustic excitation sources or other gases for flame tests.

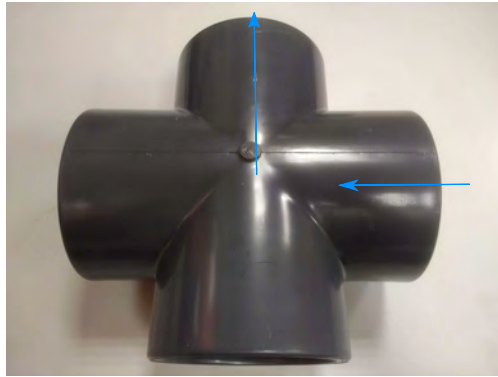


Figure 2.6: Second PVC cross. The blue arrows indicate the flow direction after being assembled in the setup.

Excepting the end in which the stagnation chamber is connected, all ends are sealed with a combination of a blind flange and a sleeved flange. The sleeved flange can be directly fitted into the PVC cross, and it can be fixed with the blind one by means of a series of bolts, with their corresponding bolts and washers.

An impinging plate (Figure 2.8) is attached internally to the blind flange that holds the hose that is connected to the mixing chamber. This plate consists on a 40 mm cap glued to a segment of pipe that is also fixed to a 40 mm nominal diameter sleeved flange. This flange is glued on the bigger blind flange, and has gone under some machining in order to make the contact face as flat and smooth as possible (The contact face is seen in figure 2.7). It was also machined to fit inside the PVC cross, as the external diameter of the flange was too big.

This impinging plate serves the purpose of avoiding a direct flow from the main pressure line to the stagnation chamber. This is why a number of holes (With its measures shown in 2.10) has been drilled radially around the lid, in order to let the flow exit the impinging plate and go towards the stagnation chamber with less velocity.

To prevent choking, the total area of these holes must be equal or bigger than the exit area of the nozzle, which has an exit radius of 5.5 mm. Thus, the machined area was set to approximately 95 mm^2 .



Figure 2.7: Top view of the machined sleeve flange.



Figure 2.8: Complete impinging plate.



Figure 2.9: Machined lid of the impinging plate.

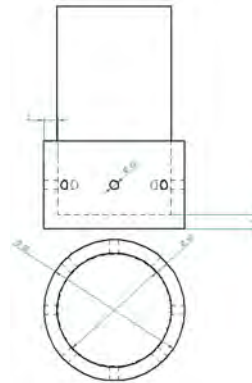


Figure 2.10: Drawing of the machined lid.

The machine used for the holes, the angle variator (Fig. 2.12), has a determined set of angles in which it can rotate. One of these values is 36, so it can rotate the clamped piece in stops of 36 degrees. Taking this into consideration, fixing the number of holes at 10 made the machining much easier. This angle variator was assembled into the miller in order to make the holes (Fig. 2.11). An external milling was used in the lathe to reduce the outer diameter.



Figure 2.11: Miller used to drill the impinging plate.



Figure 2.12: Angle variator that goes attached to the miller.

The flanges have three cavities on the shared face that allow the fluid to be sealed within the setup. This was achieved by placing silicone sheets between both flanges, and then squishing them by applying a relatively high pressure to the bolts when they are being screwed.



Figure 2.13: Top view of a sleeved flange.



Figure 2.14: Bottom view of a sleeved flange.



Figure 2.15: Bottom view of a blind flange.

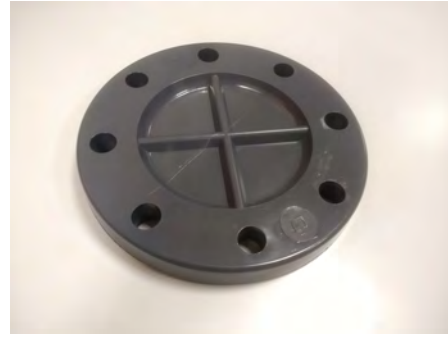


Figure 2.16: Top view of a blind flange.

Figures 2.13 to 2.16 show the flanges that were used to seal the chamber. One of these blind flanges has been machined in the same fashion as the 40 mm caps from the mixing chamber, with the difference that some "nerves" present in the face (The ones that can be seen in Fig. 2.17) had to be cleaned in order for the hose's end to fit correctly. The end of the cross that is in front of this one is connected directly to the stagnation chamber, as the 110 mm diameter PVC tube used is the male counterpart of the PVC cross. The nerves were cleaned with a face milling in a lathe, with fixed tooling and rotating piece.



Figure 2.17: Top view of the machined blind flange.



Figure 2.18: Bottom view of the machined blind flange.

On figures 2.17 and 2.18 the hole for the hose connector can be seen, as well as how the nerves have been cleaned from the top view.

2.4 The stagnation chamber

The stagnation chamber is one of the most important elements of the setup. It consists on a single PVC pipe of 110 mm of external diameter, and 103 mm of internal diameter. Nevertheless, it has to be considered that the piece is not perfect, and thus the circle has different diameters in different parts. This is why different measures are made in order to obtain a better overview of the mean radius, and the ones mentioned here are the selected representative values.

The role of the stagnation chamber is to slow down as well as reducing turbulent intensity as much as possible, while keeping a relatively uniform velocity profile.

Inside the second chamber the flow is subdued to sharp turnings, be it when exiting the impinging plate or when passing through the two sealed ends (The flow sees a kind of sudden expansion and then a sudden contraction, which produces recirculation), and this causes some turbulence in the flow, be it small instabilities or larger eddies. To palliate these effects as well as any other irregularity the stream may present, two elements were introduced inside the stagnation chamber: A wire screen and a honeycomb

A wire screen consists of a number of wires placed in perpendicular rows. Its main task is to destroy the vortical structures of the flow and obtain a more laminar-like stream, but it also tends to make the profile more uniform.

Since the drag losses that the net generates locally on the different parts of the flow in the radial direction (Of course, it also works in the azimuthal direction, but less impact is expected to be needed there) are approximately proportional to the velocity squared [2], the areas where the flow is faster will slow down more than the rest, hence achieving a more regular profile. This also means that places where more turbulence is present will have a higher impact on them.

To keep the flow from developing profile uniformities again, the screen should be placed relatively near the entry of the nozzle, although if it is too close it may not have space to completely straighten before entering the nozzle (Since the flow straighteners beark vortical structures, but still generate perturbations to the flow). The distance recommended in the literature is between 7-10 mesh lengths [2]. Taking the cell length as about 3 millimeters, the screen will be placed about 20 centimetres before the nozzle entrance.

In this setup, the wire screen is made of a mosquito net, as it is simpler and cheaper than a 3D-designed or any kind of specialized wire screen. Of course, the fact that the face that will be seen by the air is flat increases the total drag of the screen, but as already mentioned, the total head loss is not regarded as a problem in this first design of the facility.

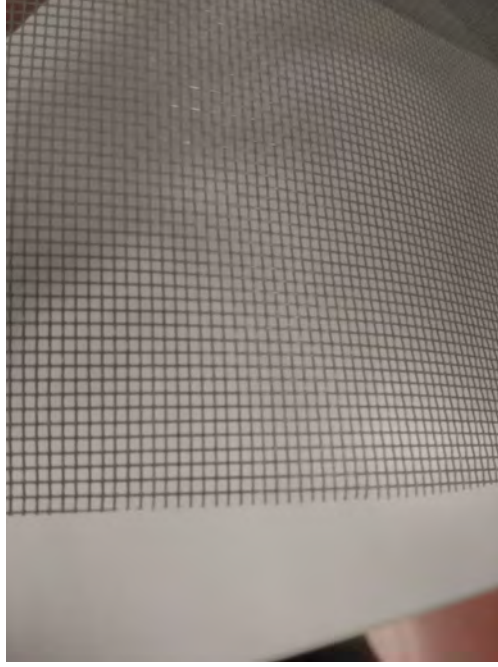


Figure 2.19: Mosquito net.

One of the main parameters that defines how good a wire screen will perform is the so-called porosity, describing the apparent area that is free from the point of view of the flow, with respect to a free way (Or a vanishing screen, in other terms). The formula that Barlow et al. ([2]) propose for the porosity is:

$$\beta_s = (1 - d_w \rho_m)^2 \quad (2.1)$$

where d_w is the wire diameter and ρ_m is the inverse of the width of a square mesh cell. If β_s is 0, the area is completely blocked. Conversely, a porosity of 1 would indicate there is no screen on the way. A value higher than 0.57 is recommended to avoid flow instabilities in the screen.

The mosquito net used presents a wire diameter of 1 mm and a square width of 5 mm, thus a ρ_m of 1/5. This means that the porosity is 0.64, which is over the recommended value and hence valid for the facility.

In order to install the screen within the stagnation chamber, a frame is designed and 3D-printed, and the net can be attached to it. This frame is a single 1 cm tall circle, with a radius of 102,5 mm, such that it has a certain clearance with the PVC wall. In this way, it is ensured that the frame will fit the hole while having a small clearance with the wall. In order to attach it, three stripes of american tape with 120° of separation between them fix the frame to the structure. This method is simple, cheap and will be able to withstand the low stresses that the elements will be subject to.

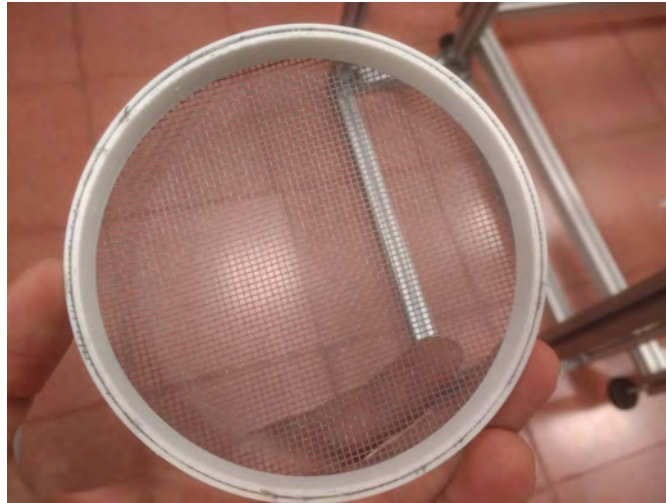


Figure 2.20: Mosquito net already mounted within the frames.

The removal of the frame for cleaning the net, or substituting it with a new one, can be achieved simply by removing the tape and then carefully pushing the frame out with some element, since it presents some resistance to the movement because the clearance is very small. Afterwards, a cleaner can be used to eliminate any adhesive remains inside the chamber.

The role of the honeycomb is to act as a flow straightener. This element is longer in the axial direction of the flow, and thus the vortices that induce velocity in azimuthal and radial direction have more time to collide with the walls of the honeycomb and then loose their intensity. This, as well as making the velocity profile have a predominant value in the axial direction, also helps destroying turbulence, in a similar fashion as the wire screen does.

The honeycomb is a more difficult and expensive element to obtain, and hence the solution chosen is to design the part with a computer and use the 3D printer. The software SolidEdge V19 allowed to design the honeycomb and export it with good quality into a format that could be inputted into the 3D printer's software.

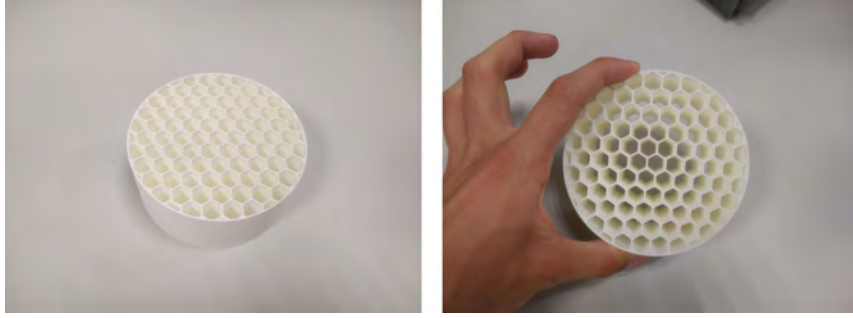


Figure 2.21: Two different views of the printed honeycomb.

Again, the parameter taken into consideration for its performance will be the porosity. Nonetheless, there is less literature about this, and, even though Barlow et al. ([2]) make use of this parameter in their book, there is no explicit formula to be found. Hence, an approximation is done as the following:

$$\beta_h = \frac{D^2}{C^2} \quad (2.2)$$

where D is the distance between two parallel sides of a hexagonal cell, and C is the distance between the centres of two consecutive cells. The distance D is measured between the inner sides of the hexagon's thickness, and hence it takes this parameter into consideration.

The parameters D and C are 9.53 and 10.4 millimeters, respectively. Inputting this into the formula gives a porosity of 0.84, which is in accordance with Barlow et al. ([2]) that suggests the porosity to be in the vicinity of 0.8 to maintain the losses around 0.5.

2.5 The nozzle

The nozzle is also one of the most important parts of the setup. Its objective is to accelerate the flow at the exit of the stagnation chamber, while keeping the velocity profile as uniform as possible, avoiding any boundary layer separation. The velocity profile uniformity is important for the coherent structures to form as they should.

If the profile is not uniform or perturbations of a noticeable order of magnitude are present, the flow structures could appear already disturbed and hence disappear earlier, having an undesired behaviour for their study. Hussain [23] summarizes the different magnitudes (Like the mentioned uniformity of the velocity, or the three characteristic thicknesses from the boundary layer) that are believed to be most important to take account of as initial conditions.

It is worth noticing that Hussain does not mention the Reynolds number among these magnitudes, as there are some authors that argue the importance of the Reynolds number in the behaviour of the jet, due to its influence on the interface between the ambient air and the jet air ([41], [15]).

Since the nozzle has to be specifically designed for the purpose of obtaining a uniform velocity profile, it will be created through 3D printing. There a vast literature regarding the design of nozzles for this purpose. In this project, the method explained in Mikhail's paper [28] will be the one followed.

An important aspect of the nozzle design is the contraction ratio, as higher contraction ratios imply less turbulent intensities. Hence, a big contraction ratio would allow the structures to form unperturbed. A big contraction ratio can be easily obtained by reducing the exit diameter of the nozzle, which would also mean that, since the different magnitudes are generally scaled with this diameter in the literature, one could study longer axial distances downstream. Increasing the contraction ratio in this way also guarantees the outer diameter to not increase, being this an advantage for laboratories with limited space.

The counterpart of this is that the Reynolds number would be smaller. Recalling its formula:

$$R_e = \frac{U_{exit}D}{\nu} \quad (2.3)$$

and knowing that U_{exit} and ν , the exit jet velocity and the air kinematic viscosity respectively, are fixed, it is clear that a very reduced radius would not yield a turbulent flow, therefore making the nozzle unable for this kind of experiment.

Thus, the contraction ratio was selected considering both a Reynolds ratio that ensured a turbulent flow, while keeping the diameter not high enough for a contraction ratio of 10 to yield an acceptable inlet diameter for the nozzle. This value is generally used in the literature, with just one difference: The ratio selected is usually based in areas, and

not in diameters (Or ratios). This means that the chosen ratio would be equivalent to a 100 contraction ratio if the areas had been used as the reference magnitude.

Due to convenience at the moment of procuring the PVC materials, the ratio had to be adjusted, being kept near 10. The reason for this change is that the internal diameter of the tube used for the stagnation chamber was 103 mm. Thus, in order for the flow to see a constant section, and not impact on a wall of the nozzle (Or expand to it, if it were bigger than the stagnation chamber), the nozzle was adapted.

The following table summarizes the relevant geometric data about the nozzle.

| | |
|-----------------------|-----------|
| Nozzle Inlet Diameter | 103 mm |
| Nozzle Exit Diameter | 10 mm |
| Contraction Ratio | 10.300 |
| Contraction Length | 54.075 mm |

Table 2.1: Characteristics of the nozzle

The length of the contraction has been obtained by multiplying the inlet radius times 1.05, as the literature suggested [28].

Once given the desired geometrical characteristics, the next crucial point was defining the shape of the nozzle. This defines the behaviour of the flow during the discharge, hence determining the wall pressure development and boundary layer separation, as well as the velocity profile. Mikhail ([28]) suggests using the distribution shown in eq. 2.4 for the second derivative of the function that gives as an output the radial coordinates of the nozzle wall.

This distribution (Observable in figure 2.22) is divided between the inlet and the exit section, which are divided by the only inflection point present in the curvature of the wall (This inflection point can of course be changed by adjusting the parameters of the formula).

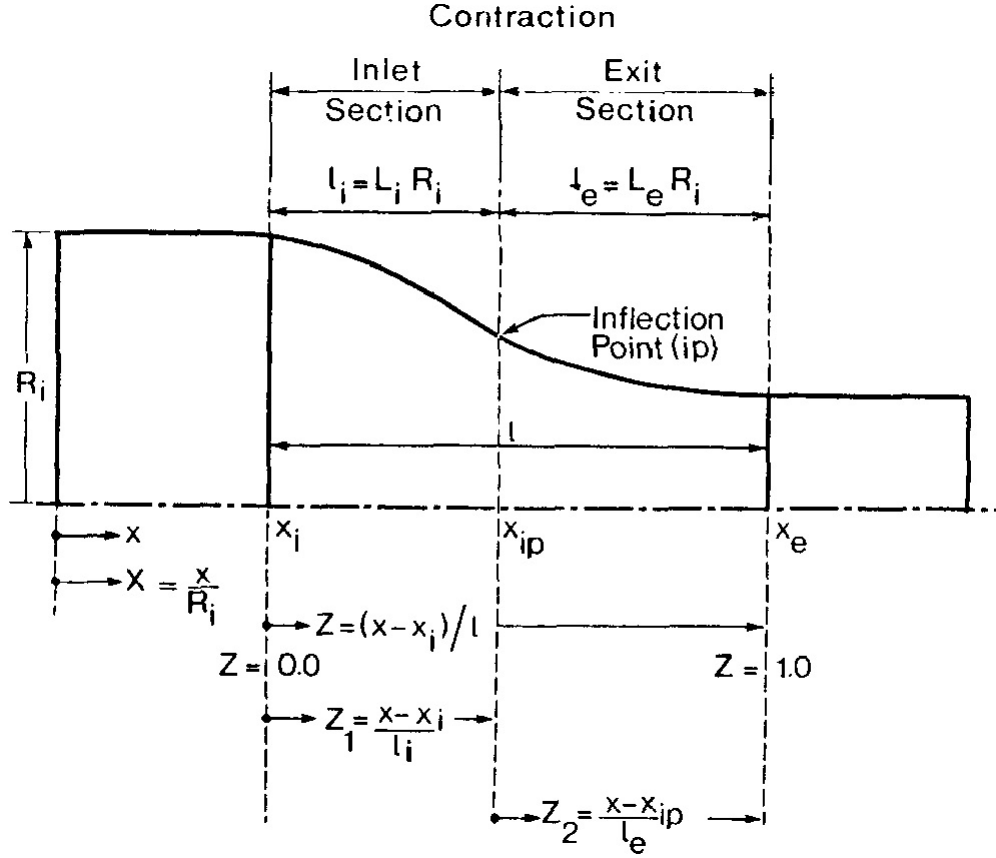


Figure 2.22: Nomenclature followed, extracted from [28].

$$R''_{\text{Inlet}} = -A_1(l + B_i Z_1) [\text{Sin}(\pi Z_1)]^{N_i} \quad R''_{\text{Exit}} = -A_2(l + B_e Z_2) [\text{Sin}(\pi Z_2)]^{N_e} \quad (2.4)$$

To define the inlet and exit ratio, parameters A_1 and A_2 are used. They also serve to define the zero wall slope condition at the ends of the nozzle. The B coefficients control the positions of the peaks of the distribution. It shifts the sinusoidal functions that are being matched to the left or the right of the x -axis (This axis can be seen in figure 2.23).

The parameter l is the sum of the inlet and exit length, that is, $l = l_i + l_e$. N_i and N_e can be tuned to change the pointedness or squaredness of the functions, making the derivative more or less steep.

Finally, the variables Z_1 and Z_2 are the axial coordinates of the position of the wall, such that $0 < Z_1 < l_e$ and $l_e < Z_2 < l$.

This means that the position of the inflection point can be controlled with the B factors and the smoothness of the sine functions (And thus the smoothness of the wall) with the N factors.

The factors A were controlled by means of an optimization that reduced an error function that forced the exit radius to be the desired, as well as the exit slope to be 0 (That is, that the exit is parallel to the axial direction). The rest of parameters could be changed prior to this optimization, allowing to obtain different sets of nozzles with the appropriate dimensions and different wall shapes.

The values selected for these parameters are summarized in the following table:

| | |
|-------|-------|
| A_1 | 1.34 |
| A_2 | 11.44 |
| B_e | -1 |
| B_i | 1.5 |
| N_e | 3 |
| N_i | 1 |

Table 2.2: Coefficients defining the nozzle wall shape.

These agree with most of the design parameters chosen by Mikhail ([28]). B_i and N_e are in the design limits beyond which no appreciable improvement is present.

The parameter B_e was chosen negative to improve the uniformity of the velocity profile, as the value of 0 used by Mikhail ([28]) did not guarantee a derivative of the wall shape function of 0 in the exit, meaning that the nozzle exit may have had an angle in its final section. The counterpart of this parameter being negative is that the margin of safety for boundary layer separation is lower, but the overall smoothness of the wall shape obtained with the rest of parameters and the low velocities should make up for that.

The parameter N_i , however, is very different from what Mikhail suggests (In the paper, this author chose 0.01 whereas here is 1). The biggest difference for this is that with Mikhail's value the derivative of the wall shape function was too sharp at some points, which could lead to potential flow separation. Thus, a value of 1 to obtain a smoother derivative was chosen.

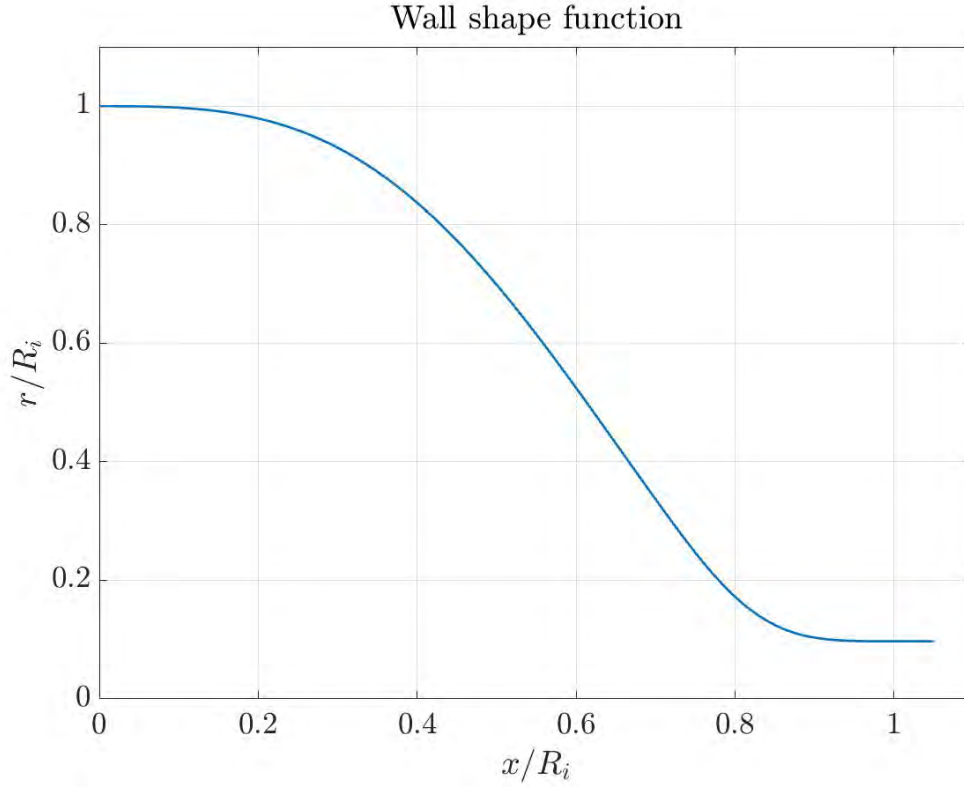


Figure 2.23: Wall shape function.

The wall shape obtained is depicted in Fig. 2.23, as well as the wall derivative function in Fig. 2.24. The latter indicates how the smoothness of the former is, showing how fast the wall shape varies. Here it can be checked that the point with the most slope of the wall coincides with the inflection point, which was determined at 0.65 radiuses. Since the y-coordinates of the wall shape are always decreasing, the derivative is of course always negative.

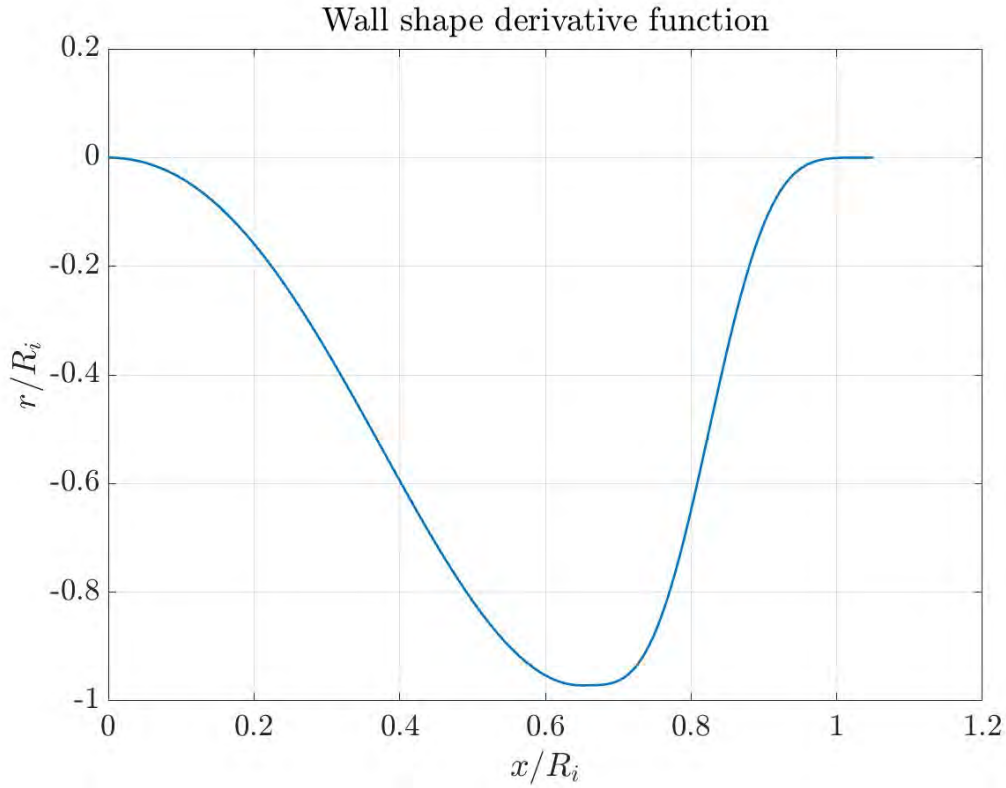


Figure 2.24: Wall shape derivative behaviour.

Once it was obtained, the next step was to design the 3D model.

2.5.1 The 3D printing

Designing the 3D model was another important part of the nozzle procurement. The output of the Matlab code was a series of points containing the coordinates of the nozzle walls in a 2D plane, and a 3D version of the nozzle was built using SolidEdge in order to test it.



Figure 2.25: Top view of the printed nozzle

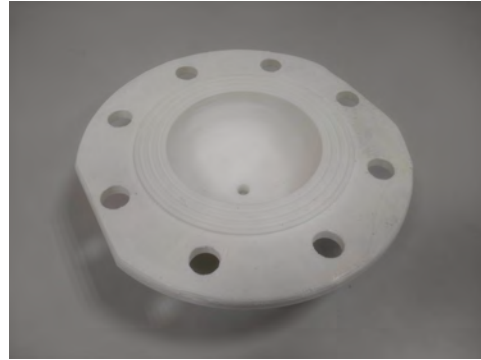


Figure 2.26: Bottom view of the printed nozzle

However, 3D printing has some drawbacks, and in this case the nozzle was not perfectly printed. The time the machine takes to manufacture a piece, and hence the hot plastic is cooled down by itself in the cage, while the rest of the piece is being created. In this case, it produced a deformation in the nozzle wall, as the weight of the nozzle parts that was above the deformed area was too much for the hot plastic to bear.

In Fig. 2.28 this defect can be appreciated. The initial part of the nozzle, that is directly connected with the flange (The part at the left of the picture) is seen to not be perpendicular to the flange, but rather have an angle. This can be appreciated comparing figures 2.23 and 2.28. The wall shape in the x-axis from figure 2.23 is clearly different from what it turned out to be in figure 2.28.



Figure 2.27: Side view of the printed nozzle.



Figure 2.28: Close-up of the wall shape. The deformed part can be appreciated here, at the left-most of the nozzle wall.

There is the possibility that by slowing down the printing, enough time could be given to the plastic to gradually cool down while bearing less weight, therefore avoiding the deformation. However, the time constraints in the development of this project made this option not feasible.

Another issue encountered with the nozzle was inherent to the method the printing machine uses to fabricate the piece, which does not leave a smooth surface, but a rough one. This could potentially lead to extra instabilities in the flow, and hence acetone was used to polish the surface. However, it was not effective, and due to the risks of treating the material further, no more actions were taken.



Figure 2.29: Close view of the interior of the nozzle. The wrinkled surface can be appreciated here, which remained even after the polishing with acetone.

2.6 The supporting frame

The final part of the setup is the structure that holds the stagnation chamber and everything that comes directly attached to it. Its purpose is to keep the nozzle pointing upwards, perpendicularly to the floor, while providing stability to the whole chamber in order to avoid possible vibrations to affect the results of the tests. Furthermore, it has to provide a sufficient clearance between the jet and the walls, so that it does not behave as an enclosed jet, but a free one (Or as similar as possible to one).

Taking into account the limited dimensions of the laboratory, and the fact that this laboratory is not exclusively dedicated to this test, the structure will consist on a square prism, with a side of 1 meter and a height of 2 meters.

At approximately 75 cm over the ground, the profiles make not a square, but only two sides of it. The other two sides are attached closer, making a place where a sleeved flange can be fixed to. This allows to put the nozzle in place.

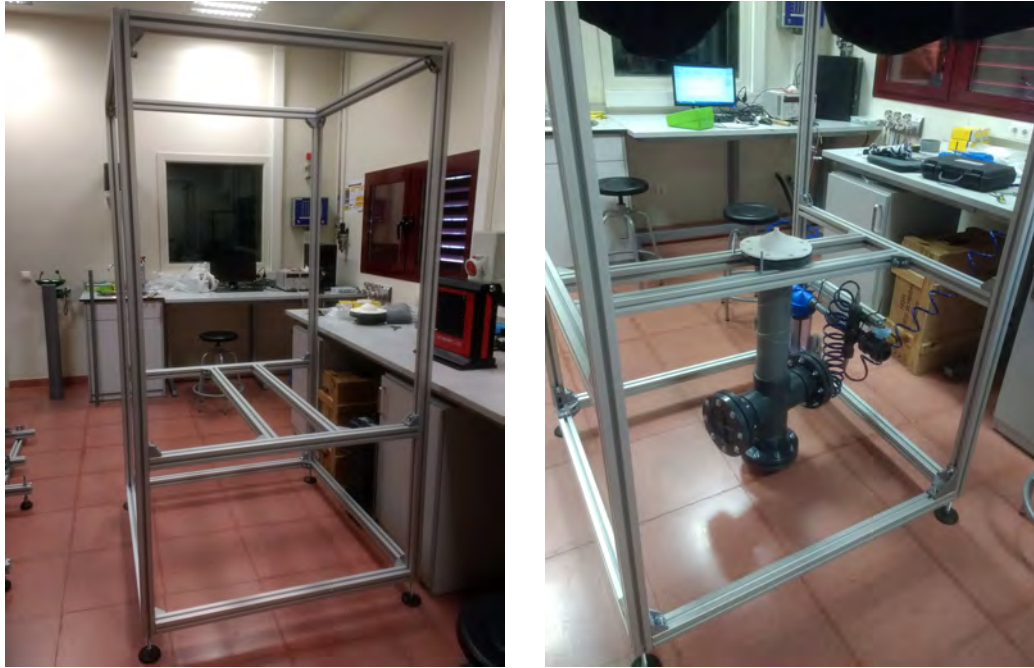


Figure 2.30: Empty mounted structure. Figure 2.31: Setup with the nozzle mounted in the structure.

Note that Fig. 2.30 shows an older version of the structure. In the final one, the middle frame was moved upwards to fit the setup, as can be seen in Fig. 2.31.

The nozzle in Fig. 2.31 is fixed to the chamber with the use of a sleeved flange, and it is screwed to this flange. However, since regular bolts are too short, threaded rods are used to attach both of the elements and the aluminum profiles. Threaded hammer heads can be screwed into the ends of the rods, to behave as stops in the profiles. The final result is simply a very long hammer-headed bolt.

The structure is mainly made of aluminum profiles that have a square-like cross-section, with a side of 4.5 centimetres. The cross-section is not closed, as it has rectangular grooves in each of the sides. These grooves allow to fix a variety of elements by putting a hammer head bolt, putting it perpendicular to the groove's direction, so that it cannot move outside of the profile. Figures 2.32 and 2.33 illustrate this groove better.



Figure 2.32: One of the sides of the profiles.

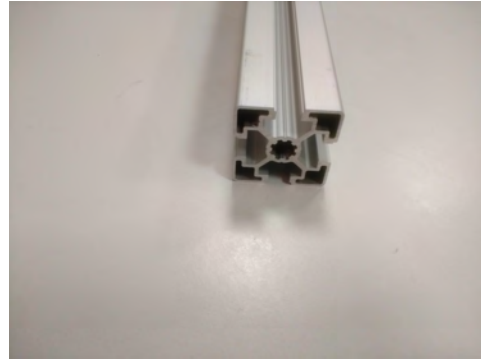


Figure 2.33: Front view of the profile.

The profiles are fixed with each other with brackets. These, at the same time, are attached to the profile by means of screws and a special nut that already has a washer incorporated.



Figure 2.34: One of the brackets used for the profiles.

In order to correctly provide stability to the structure, the profiles have to be fixed within the same plane. Figure 2.35 depicts how the brackets should be assembled.



Figure 2.35: Mounted set of brackets and profiles.

Finally, the profiles present an end in which an M8 thread has been machined. This serves the purpose of attaching wheel or feet to the structure. Since this structure must stand still, feet will be used here.



Figure 2.36: One of the feet of the structure.

The foot consists of a basis of rubber that is attached to an encasing of hard plastic. This plastic has a hole for the thread of the foot, which allows it to rotate slowly (It presents some moments counteracting the movement thanks to friction). All these elements are fixed together through pressure, making the foot robust.

The deformable rubber, the rotation of the bolt and the capacity to easily be screwed up or down allows these feet to provide stability even if the floor is not uniform. However, attention had to be put in order for the structure to remain parallel to the floor at the time of the test.

Lastly, all the structure was covered with a blanket, so that the laser light does not go out from the test area. For this purpose, black felt, that has good light absorption and relative endurance of high temperatures, was chosen.

The fabric width is 90 centimetres, and hence to cover up the 1 meter sides, sets of two were used, yielding 4 pieces of 2.5 meters and 2 pieces of 6 meters to cover the complete structure. The extra blanket will help covering the structure when the laser is put inside the blanket, as part of it has to be kept outside to allow its operation. Moreover, keeps the particles from escaping the setup and spreading over the laboratory, making the experiment cleaner and reducing any hazards that the seeding could cause.

The ventilation of the setup is carried out simply by opening the laboratory windows. Since the seeding is not hazardous and it fills the room at a very slow rate, using the windows is enough for the ambient not to be filled with the seeding.

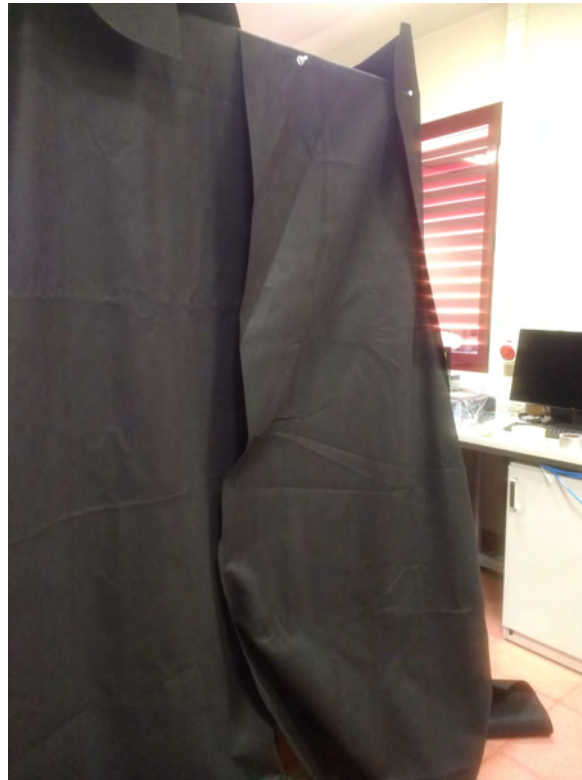


Figure 2.37: Blanket mounted in the structure.

Chapter 3

Experimental procedure

The testing procedure consists on a series of steps that allows the user of the facility to obtain the PIV results to be post-processed. Under this section, a review of the basis of how the PIV works, as well as the sensors needed to take the adequate measures will be shown. Lastly, the process followed to obtain the data analyzed will be explained.

3.1 Operating principles of PIV

As the word "velocimetry" suggests, the point of Particle Image Velocimetry (PIV for short) is obtaining the velocity field of the flow of matter. This allows the study of a variety of turbulent magnitudes that are of interest for this field, such as the so-called Reynolds stresses.

The first step of the PIV is to seed the flow. Thanks to the good light scattering properties of some elements, putting particles inside the flow allows to observe its structure while using an amount of seeding small enough such that the flow is not perturbed.

The recommended proportion of tracer particles for gas flows is $\frac{m_{seeding}}{m_{fluid}} \ll 10^{-3}$ [36]. Furthermore, the diameter and density of the particles must be taken into consideration, with the aim of them following the streamlines of the flow as smoothly as possible.

This behaviour can be measured by means of the Stokes number, defined as:

$$S_k = \frac{\tau_p}{\tau_f} \quad (3.1)$$

where τ_p is the characteristic time response of a single particle, and τ_f is the characteristic flow time. Scarano and Westerweel also state that a good tracking can be achieved with a Stokes number less than 0.1 [35].

In order to obtain the time response of a particle, a formula is also provided:

$$\tau_p = \frac{2}{9} a^2 \frac{\rho_p}{\mu} \quad (3.2)$$

where a is the particle diameter (usually in micrometers), ρ_p is the density of the seeding and μ is its dynamic viscosity. The seeding element used in this case will be Di-Ethyl-Hexyl-Sebacat, with formula $C_{26}H_{50}O_4$. It is mainly a biodegradable mineral oil, which is transparent and does not have an especially strong odor. It presents a molecular weight of 426.682 g/mol and a density of around 0.9 times that of water, i.e., 900 kg/m³. It has a particle diameter of 1 μ m and a viscosity of $\mu = 22 \cdot 10^{-3}$ Pa \cdot s.

Introducing these information into equation 3.2 gives a characteristic response time of $\tau_p = 9.10 \cdot 10^{-9}$ seconds.

The characteristic flow time that must be used is the so-called Kolmogorov scale. This scale is the smallest one, and it is the one that serves to measure times of the smallest eddies that one can encounter on a turbulent flow. On the other side, there is the integral scale, which is used to measure the times of the bigger eddies in the flow. These two time scales can be related by means of the Reynolds number in order to obtain an approximation [39]:

$$T_L = D/U_J \quad \frac{T_L}{T_\eta} = Re^{1/2} \quad (3.3)$$

T_L and T_η are the integral and the Kolmogorov time scales, respectively. D is the diameter of the jet and U_J is the bulk velocity, both used to estimate the large eddies scale. As will be explained in section 3.3, the Reynolds number (Re) obtained for this experiment is $18.96 \cdot 10^3$. Recalling that the diameter was 10 mm and knowing that the bulk velocity was 26.74 m/s, the obtained Kolmogorov time scale is $t_\eta = 2.72 \cdot 10^{-6}$.

The Stokes number can be calculated now, yielding $S_k = 3.35 \cdot 10^{-3}$. This number is much smaller than the recommended limit of 0.1, meaning that the seeding will be adequately following the streamlines.

In order for the seeding to be visible, a thin sheet of light is emitted, usually from a pulsating laser source, and the images are taken with a digital imaging device placed in the normal direction of the plane. For the purpose of measuring the velocity field, two consecutive photos must be taken in a very narrow window of time, letting one not only obtain the velocity field, but have a first approximation of the variation of the velocities.

Other PIV techniques include stereoscopic imaging with more than one camera, allowing to obtain the 3D flow field (Discetti and Coletti, in their review of 2018, collect a good number of the different PIV variations [33]), or taking successive images in light planes slightly shifted in the direction normal to them. A better visualization can be seen in the following figures:

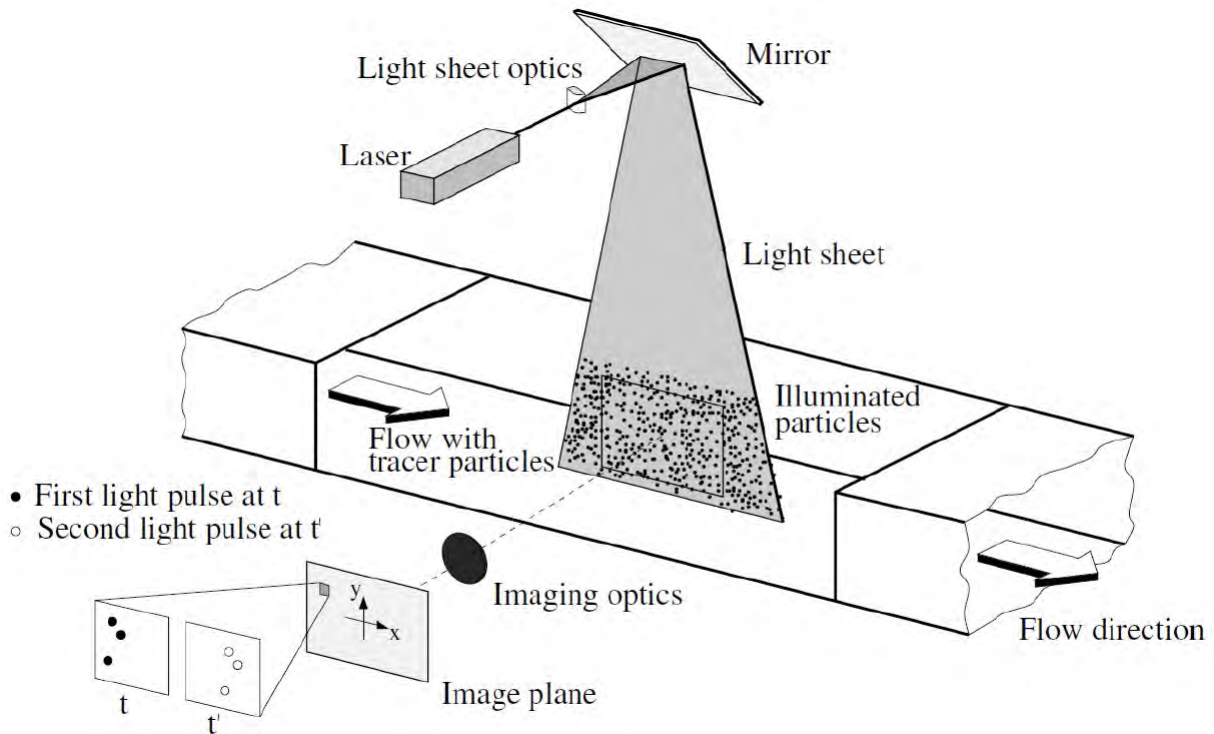


Figure 3.1: Typical PIV setup for a single-camera data measurement. Extracted from [40].

3.2 Instrumentation

The conditions of interest inside the chamber are the pressure and the temperature. With this, one can calculate the rest of interesting thermodynamic properties, as well as the flow conditions such as the Mach number. For this aim, these two properties are measured at the end of the stagnation chamber, or, equivalently, near the beginning of the nozzle.

The instruments devoted to obtain the PIV image are the laser, the camera and the synchronizer.

3.2.1 Temperature and pressure sensors

The sensors are directly fit into the stagnation chamber through drilled holes on the PVC. The small clearance plus the tape used to stick the sensors outside is sufficient to avoid air leakages.

The thermocouple is a type T thermocouple connected by an electronic reader that the university provided. This allowed to read the stagnation temperature in Kelvins.

The pressure sensor is a differential pressure Sensirion of the 600 series. It allows a pressure measurement in the range between 125 and 500 Pascals, with a zero point accuracy of 0.2 Pascals approximately. The manufacturers provided with a program to read the pressures on real time specifically designed for this sensor.

They have been set 8 centimetres apart from the nozzle. This is sufficiently far from the wire screen to not measure a flow perturbed by this screen. Also, it is far away from the nozzle inlet in order for the sensors to measure what is happening before the flow is accelerated by the nozzle.

3.2.2 The laser

The laser is, as already mentioned, a pulsed laser that emits light through a set of lens that reshapes the beam into a sheet of light with a very small out-of-plane thickness. This sheet must be perpendicular to the camera's shooting direction, so that it illuminates the seeding particles and they scatter light in the plane of vision of the camera.

The vision plane is so thin that the alignment with the mid-plane of the jet crucial.

Its main features are listed in the table below:

| | |
|----------------|-----------------------------|
| Brand | Big Sky Laser CFR400 ND:Yag |
| Energy | 230 mJ/pulse |
| Pulse duration | 3 ns |

Table 3.1: Laser characteristics.

The lighting has to be correct, and a combination of lenses is needed in order to transform a light beam into a proper light sheet. Once the lenses and the position of the light sheet are fixed, the laser can be left untouched for all the tests.

3.2.3 The camera

Perpendicular to this light sheet is the camera, held by a tripod. Its main features are shown in the next table:

| | |
|-------------|-------------------------------------|
| Brand | Andor <i>ZylaTM</i> 5.5 |
| Resolution | 5.5 MP in a 2560 x 1200 pixel array |
| Sensor size | 16.6 x 14 mm |

Table 3.2: Camera characteristics.

In order to use the camera, an optical calibration has to be carried out. For this, a target was printed and used to know how to pass from the distances in the image, measured in pixels to the actual distances, measured in centimetres in the target. The target has a grid of 5 cm square cells filled with points that are 1 cm away from each other in both directions of the plane. One of the reference lines is placed in the middle of the nozzle and the image captured by the camera is centered in that line.



Figure 3.2: Calibration target for the camera.

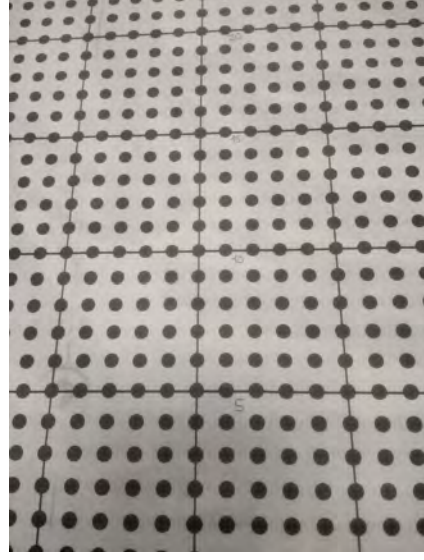


Figure 3.3: Close-up of the target.

Lastly, a synchronizing device is used to make sure that the light pulses and the camera captures at the same time.

3.3 Data measurements

As already mentioned in section 2.4, the intended Mach number at the nozzle exit was 0.1. However, for safety reasons due to the pressure appearing to be too high for the setup, the Mach number achieved in the end was of approximately 0.084, calculated with:

$$M = \left(\frac{2}{\gamma - 1} \right)^{1/2} \left[\left(\frac{p_c}{p_a} \right)^{(\gamma-1)/\gamma} - 1 \right]^{1/2} \quad (3.4)$$

Where γ is the usual air constant with value 1.4, p_a is the ambient pressure and p_c is the chamber stagnation pressure. Together with:

$$V_{exit} = M \cdot \sqrt{\gamma R T} \quad (3.5)$$

with $R = 287 \text{ J/KgK}$ and $T = 298 \text{ K}$, the theoretical velocity obtained is 27.68 m/s . This was confirmed by measuring the velocity with an anemometer, which gave an exit velocity of approximately 25 m/s right before the first run.

Considering this velocity, the nozzle diameter of 10 mm and the air properties at room temperature ($\nu = 1.46 \cdot 10^{-5} \text{ m}^2/\text{s}$), the Reynolds number that was obtained was $18.96 \cdot 10^3$, assuring that the jet was actually turbulent.

The different values of pressure and temperature of interest did not remain completely constant through all the experiments, but the variation was small and did not compromise the results of the tests. These values are summarized, for all the different runs, in the tables below.

Note that the chamber pressure was measured as the differential pressure with the ambient one, and hence it is expressed in the tables as "Pressure difference", meaning that the value appearing there is the extra pressure inside the chamber, compared to the ambient one.

| Run 1 | |
|-----------------------------|----------|
| Chamber Temperature | 297,1 K |
| Chamber Pressure difference | 506.5 Pa |
| Ambient Temperature | 296.7 K |
| Ambient Pressure | 933 hPa |

Table 3.3: Data in Run 1

| Run 2 | |
|-----------------------------|----------|
| Chamber Temperature | 298,6 K |
| Chamber Pressure difference | 505.2 Pa |
| Ambient Temperature | 299.3 K |
| Ambient Pressure | 933 hPa |

Table 3.4: Data in Run 2

| Run 3 | |
|-----------------------------|----------|
| Chamber Temperature | 300,1 K |
| Chamber Pressure difference | 490.5 Pa |
| Ambient Temperature | 301.1 K |
| Ambient Pressure | 932 hPa |

Table 3.5: Data in Run 3

| Run 4 | |
|-----------------------------|----------|
| Chamber Temperature | 300.5 K |
| Chamber Pressure difference | 492.1 Pa |
| Ambient Temperature | 301.3 K |
| Ambient Pressure | 931 hPa |

Table 3.6: Data in Run 4

| Run 5 | |
|-----------------------------|----------|
| Chamber Temperature | 300.9 K |
| Chamber Pressure difference | 485.5 Pa |
| Ambient Temperature | 302.3 K |
| Ambient Pressure | 931 hPa |

Table 3.7: Data in Run 5

Lastly, it can be seen in figure 3.4 how the pictures were taken on each run. As it is schematic, the distances do not correspond to the actual relative distances that were used in the tests. Regardless, it shows the beginning and ending of the vision field of each run, indicating the axial length corresponding to each point. Lastly, the reference system of the plane can be seen in the bottom left corner, where the directions of x (The axial coordinate) and r (The radial coordinate) are indicated.

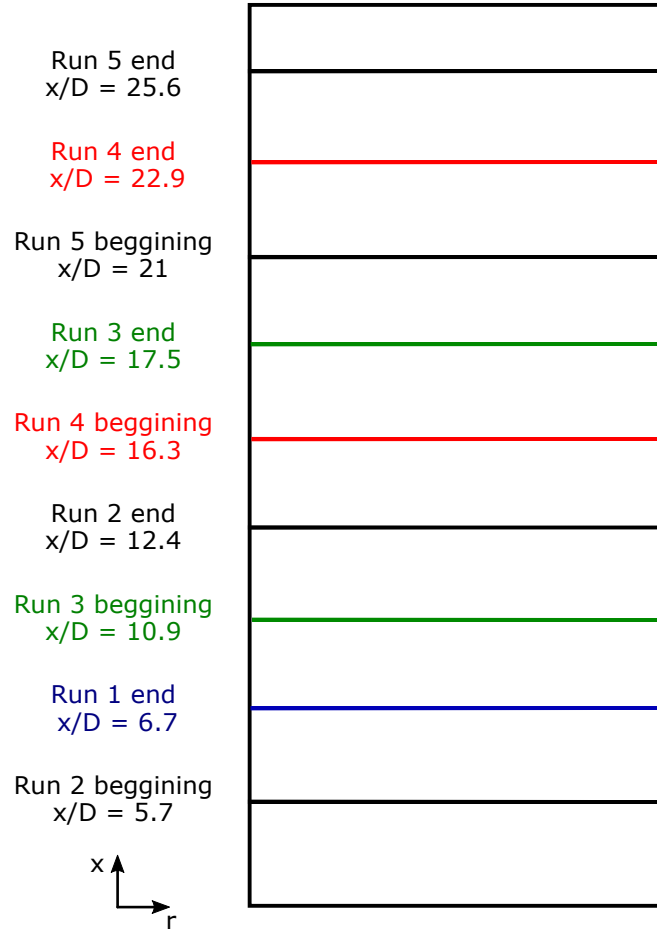


Figure 3.4: Schematic of the field of vision of each of the pictures taken, along with the reference axis.

3.4 Data treatment

The obtained data after PIV processing were 2000 velocity fields per run. The average velocity field can be obtained if all of these image sets are averaged after obtaining the velocity field of each image set.

However, prior to obtaining the velocity field, a pre-processing was done to the pictures. This refinement consisted on eliminating the background noise, which was the extra light present at the points that did not represent any seed particle. This is, making the dark background darker by eliminating the light that was present due to filtrations through the blanket or reflections that were not possible to mitigate.

For this "noise cleaning", a process called eigenbackground removal was used [1]. The images were loaded as matrixes containing the information of the pixels of the image. The code ran through all the elements of the matrix, detecting the amount of light intensity corresponding to each pixel of the image, distinguishing between seeding and background pixels. This allows the program that calculates the velocity field to have a clearer idea of where the particles are located, calculating the velocity fields with more accuracy.

The next step was to use an algorithm to calculate the velocity fields. This algorithm would read every set of two pictures and compare them in order to generate a compiled one containing the contour of how the particles have moved during the time step of the two pictures.

The working method of the algorithm was to interrogate the image using windows of a user-given size, with an eligible overlap. After going through all the pictures of a run, the algorithm would make the average of all the obtained fields and produce a final velocity field out of all the data. This velocity field had dimensions of pixels, and could be inputted to Matlab through means of another code.

In Matlab, the analysis of the instantaneous fields obtained allowed the calculation of the mean velocities (Axial and radial), as well as of the Reynolds stresses. Different treatments were given to this data, such as passing from pixels to SI units or flipping the data that appeared reversed in the vertical axis. With this, the behaviours of these magnitudes with axial distance, half-radius calculations and self-similarity conditions could be studied by comparing the obtained graphs with the available literature, as will be done in the next section.

Chapter 4

Results analysis and comparison with literature

Since the purpose of the project is to verify that the setup works correctly, the consistency of its results will be checked with the available literature. The main source will be the book written by Pope et al, which uses the data from various sources, such as the study from Hussein et al. [25]. Due to the range of axial distances for which this project has its own data, different papers will be used to compare the figures.

The first interesting step is to put all the images together and have a look at the full jet. Since the runs were obtained separately, the different data was put together by means of Matlab, and then plotted here. Since averaging did not yield good results, the data within the overlap of two consecutive runs was substituted by interpolated values, which took both runs as a reference.

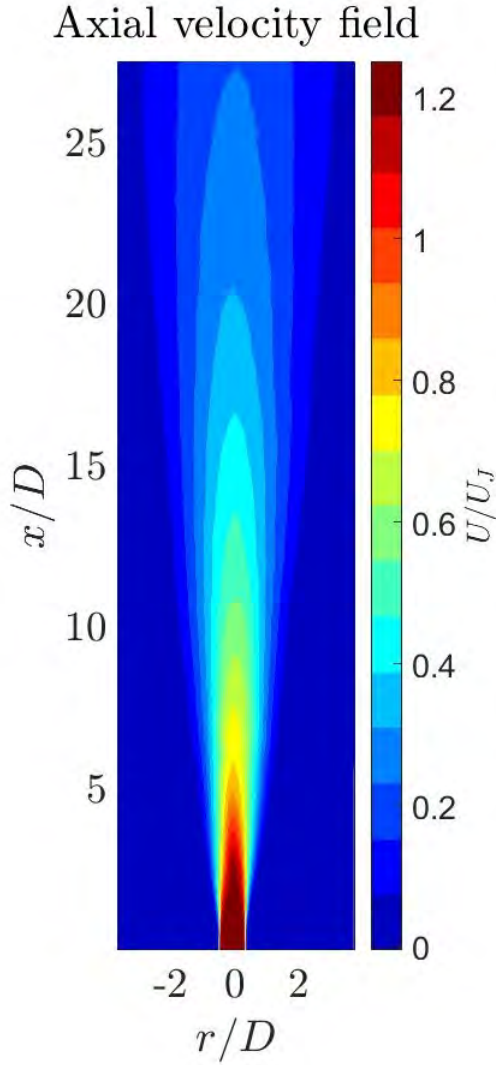


Figure 4.1: Contour of the axial velocity field

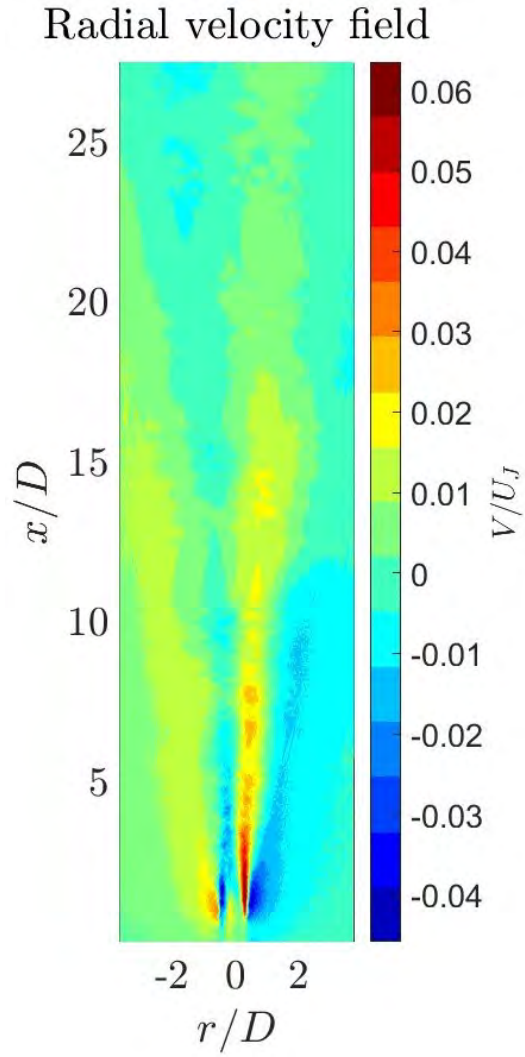


Figure 4.2: Contour of the radial velocity field

Figure 4.1 depicts the axial velocity field of the full jet. U and V are the axial and radial velocities, respectively. x and r follow the same behaviour, being the coordinates in axial and radial direction. D is the exit diameter of the nozzle (Used to scale the distances), and U_J is the bulk velocity of the jet, equal to 26.74 m/s.

It can be seen that the interpolated data generates some instabilities, but in any case the variations are not very big, and the overall result is consistent, resembling the velocity field that a free jet should have.

Notice how the field is not completely axisymmetric in the first axial distances, but rather has slightly smaller velocities on the left (Negative r/D) side. This effect is more noticeable in the first 5-7 diameters of axial length. This suggests two possible existing problems with the setup:

- The enclosing blanket is not far enough, making some recirculation appear even though the jet does indeed behave as if it were freely discharging into the ambient. Since the field is not very altered after these initial diameters, this possibility does not seem very likely.
- The blanket was not closed correctly. Even though there was no noticeable air draughts at the moment of the experiment, the possibility of air going inside the setup is still present, as the laboratory had one window opened in order to let the seed flow outside.

Furthermore, the laser was located under the blanket in the left side of the camera (coinciding with the most perturbed side), which meant that the blanket was closed slightly worse in that part. This could have allowed some kind of air stream into the setup. This would seem more likely than the first option since the upper parts of the blanket were closed better, leaving the small area that is perturbed more vulnerable to the ambient air.

This perturbation can also be appreciated looking at Fig. 4.2. It shows the radial velocity field, being positive the air moving to the right of the image.

It is now clear here that there is some kind of perturbation making the left side slower. However, the behaviour is still the expected one. The jet discharges to a slower medium, and due to the friction forces between the jet and the ambient air, the air molecules that is in the most external part of the jet gain a momentum that pushes them away from the centerline. This is the area with the most radial velocity, that can be best seen in the right part of the jet at small axial distances.

The stagnant air gains a velocity towards the jet, which can be seen as the blue area of the right (Negative velocities, i.e., air flowing towards the centerline). This confirms that the entrainment already explained in section 1.2.1 is actually happening here.

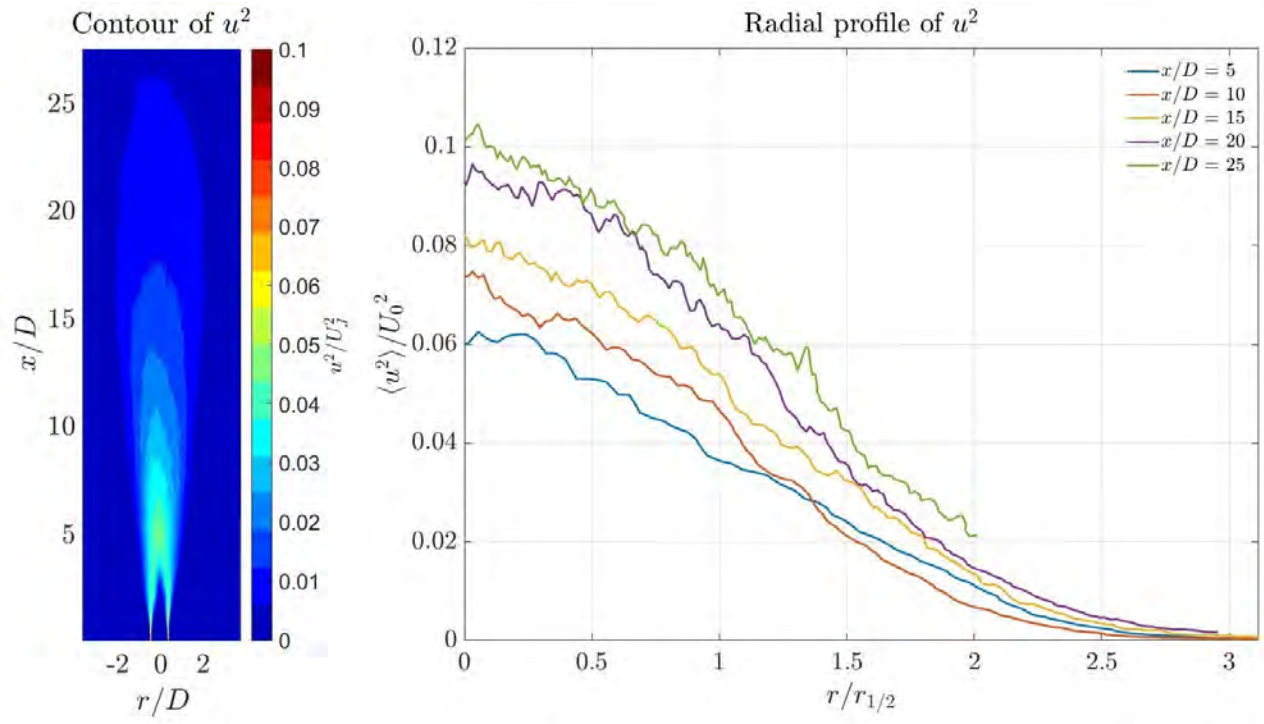


Figure 4.3: Contour and radial profile of u^2 .

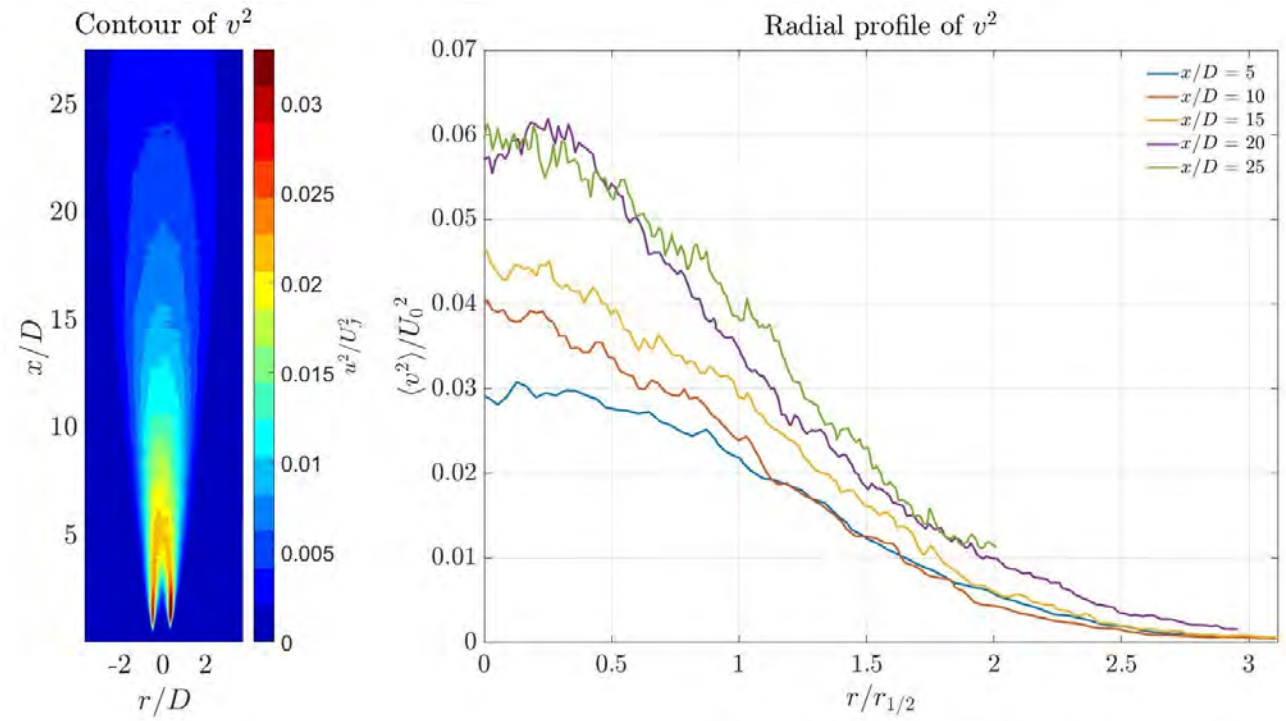


Figure 4.4: Contour and radial profile of v^2 . Some values of the contour are missing for the sake of a more clear colouring of the image.

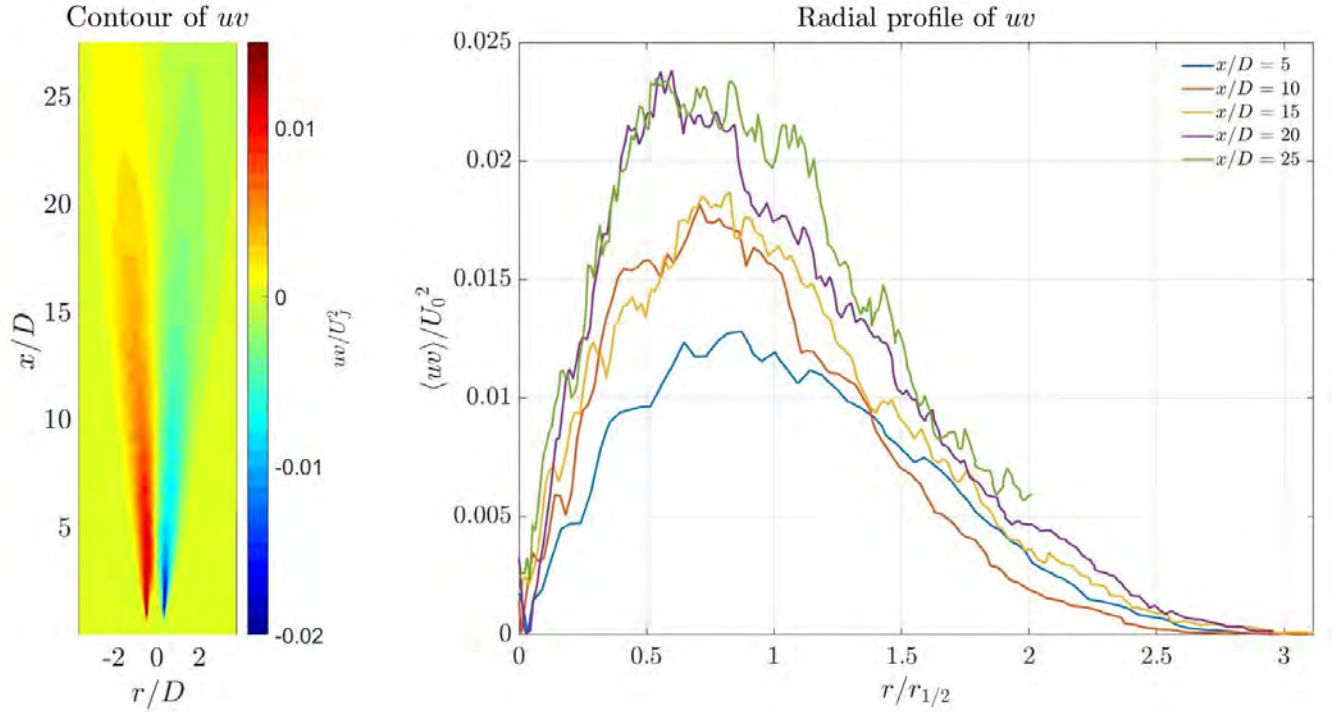


Figure 4.5: Contour and radial profile of uv . Some values (The highest positives, which go up to 0.15) of the contour are missing for the sake of a more clear colouring of the image.

In figures 4.3, 4.4, 4.5, the measurements obtained for the turbulence magnitudes, i.e., the Reynolds stresses, are shown. These show the level of correlation between the possible fluctuations from the mean velocity. A high correlation would mean that a fluctuation in one direction will have a fluctuation in the other direction indicated.

For u^2 and v^2 , this indicates the intensity of the turbulent velocity fluctuations in the axial and radial directions, respectively.

This means that the velocity will change more than it would if only statistics were the cause of the fluctuation from the field, indicating areas where the fluid is highly accelerated (Since all the values are positive, decelerating is not considered). A high uv means that the fluid tends to move radially when an axial fluctuation appears, or axially when a radial fluctuation appear.

Both u^2 and v^2 show much higher values in the areas around the center of the jet. This is due to the Reynolds stresses appearing because of the friction between the jet with the ambient air. Even though the complete jet ends up being affected from these stresses, it is not until the potential core is fully erased that this happens.

The pictures would suggest that the potential core disappears after approximately 3 diameters, which is earlier than what literature suggests (Han suggests 4/6 diameters as a distance for the potential core, which is more similar [14]).

In particular, figure 4.5 shows antisymmetry with respect to the centerline of the 2D jet. This is the expected result, as ideally the vortices should be axisymmetric, being the difference in sign due to the vortices being counter-rotating. Also, the disturbance already mentioned can be seen again here, making the values in the left side be lower than on the right side.

Recalling that this disturbance increased the radial velocities to the right, it makes sense that the left correlation between u and v has lower absolute values, as the entrainment vortex have more difficulties to form, thus making the correlations lower.

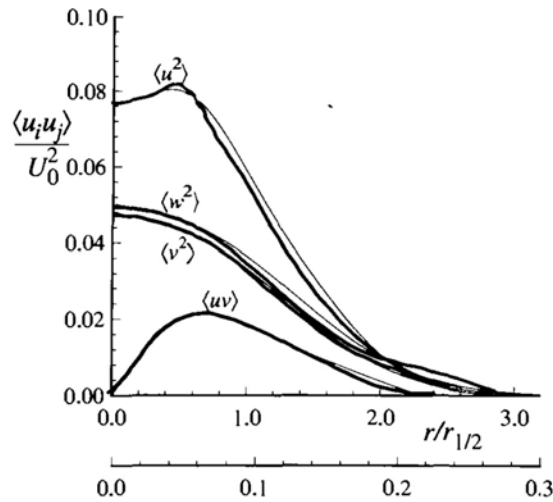


Figure 4.6: Radial profiles of Reynolds stresses as in Pope's book.

If one compares the radial profiles with figure 4.6, it can be seen that the profiles show the same behaviour, as well as having similar values. The jittering of the data might be related to the noise of the image: since the values are much lower in the turbulence magnitudes than in velocity magnitudes, the measurements are more sensitive to the noise generated. This is further indicated by the fact that in figures 4.7 and 4.8 the data set from $x/D = 25$, which corresponds to the lowest velocities, is more wavy than the other sets.

It is also interesting to note how the highest axial distances ($x/D = 20$ and 25) have the highest normalized turbulence intensities. This is due to U_0 decaying over the axial distance, which would indicate that the Reynolds stresses are quite constant over the

axial direction. The highest data approaches the self-similar region values showcased in Pope [31], which may suggest that, at some point, the Reynolds stresses intensities must also diminish to cope up with the decrease of U_0 .

Therefore, in this test the self-similarity of turbulent magnitudes has not been observed, but proof that this setup can produce it at the adequate axial distance has been provided.

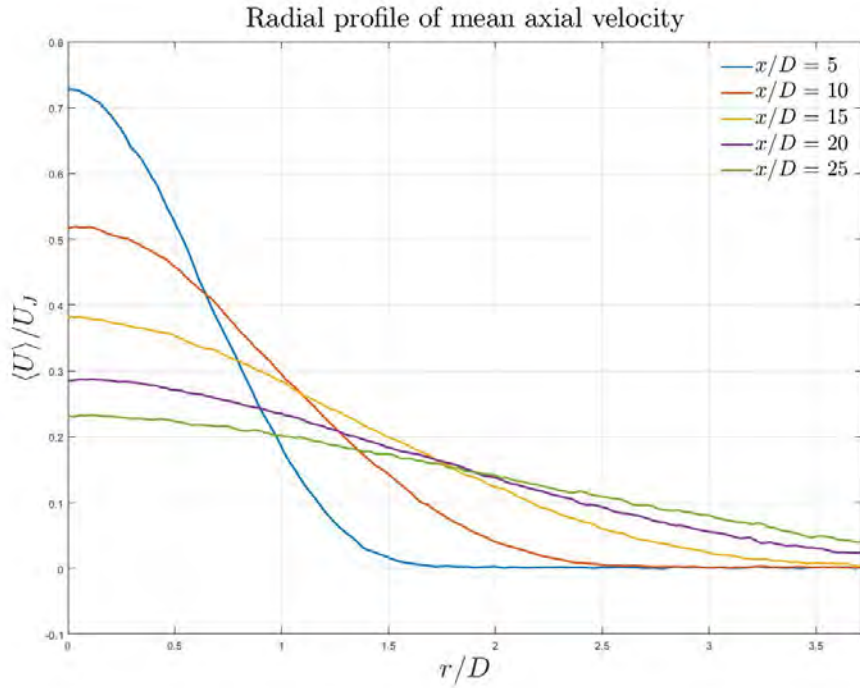


Figure 4.7: Radial profiles of the mean axial velocity.

The depiction of the radial profiles of the axial velocity makes clear how the jet decays and spreads with the velocity. The figure completely agrees with figure 1.3. It is also consistent with the rest of figures already presented, since it has the expected values and behaviours at the adequate axial distances.

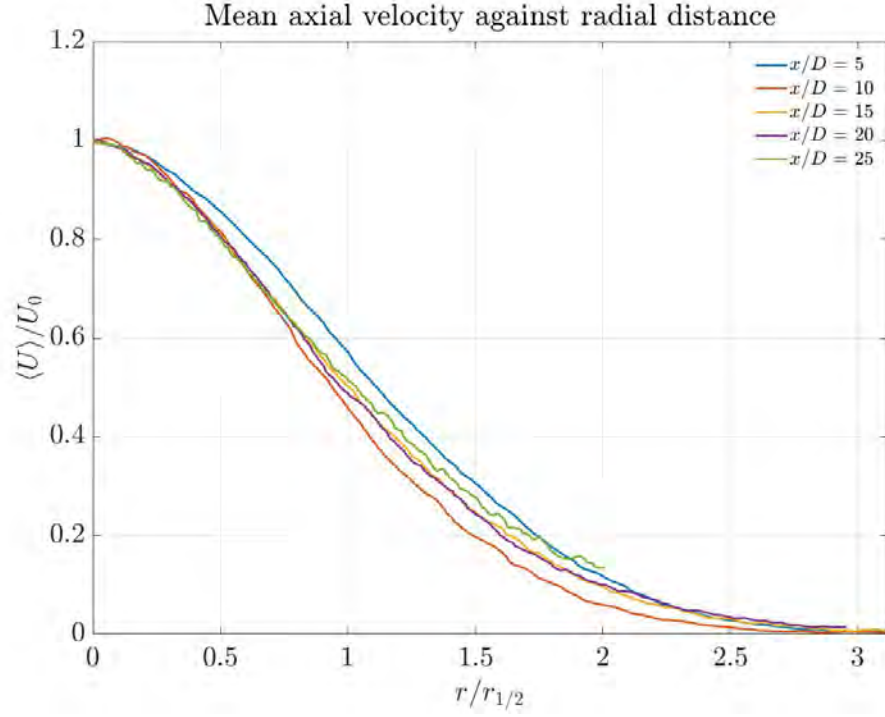


Figure 4.8: Mean axial velocity against radial distance

Figure 4.8 shows the mean axial velocity, adimensionalized with the centerline velocity, U_0 , against the radial distance, adimensionalized with the half-radius of each radial distance (That is, $r/r_{1/2}$).

It can be appreciated that the lines corresponding to $x/D = 5$ and $x/D = 10$ are not actually collapsing, but just very close. The lines from 15 and 20 diameters are in fact collapsing more into the same profile, and thus that would indicate the self-similarity begins to happen at $x/D = 15$ in the present setup.

The line from 25 diameters, even though is close to the ones from 15 and 20, it seems to be a bit separate. This could be due to the data of that run being a bit more affected by noise, and hence appearing to be more separated than it actually is due to convergence issues.

Therefore, even though it seems that the self-similarity is close to be reached, the discrepancies suggest that it is still not fully attained, and it may appear after some more axial distance, around 30 diameters on.

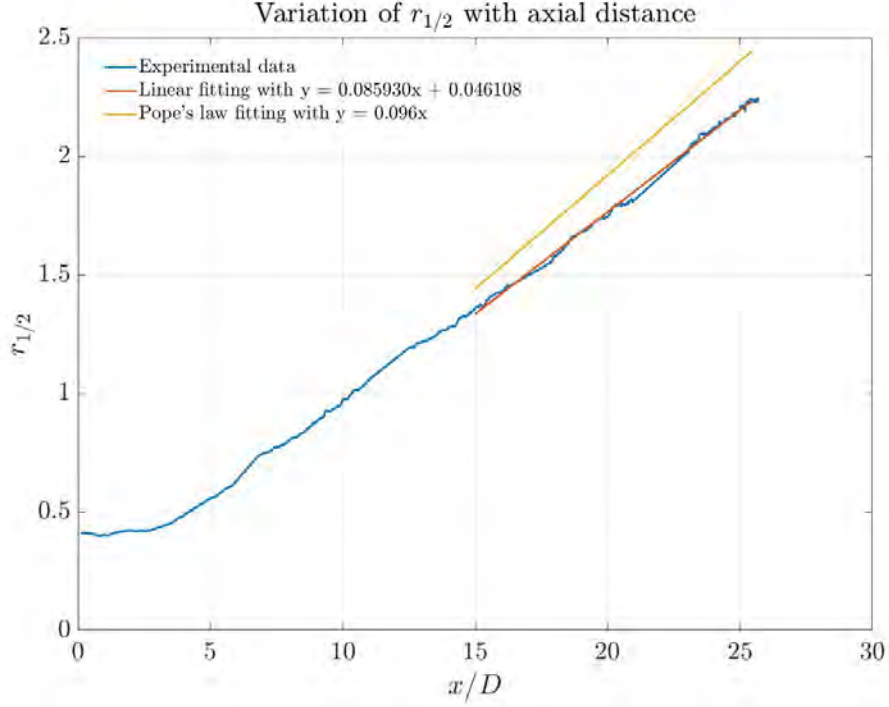


Figure 4.9: Variation of half-radius with axial distance. One of the slope values from Pope [31] is also plotted to compare. Since it is not specified in the book, x_0 is set to 0.

Fig. 4.9 shows the variation of the half-radius variation along the axial distance. As the literature shows, the variation becomes linear after the first radial distances. Furthermore, a linear fitting on the self-similar area shows that this result also agrees with the literature, as the slope of the linear fitting is 0.085. The values provided by [31] are 0.096 (From [30]), 0.102 and 0.094 (The last two from [25]), which are pretty close to the obtained fit.

The difference in the slopes is small, but very clear in the picture, where the jet of the present test is seen to decay less than the ones in the experiments from the literature.

From the self-similar distance onwards, the jet is seen to decay linearly, agreeing with the literature.

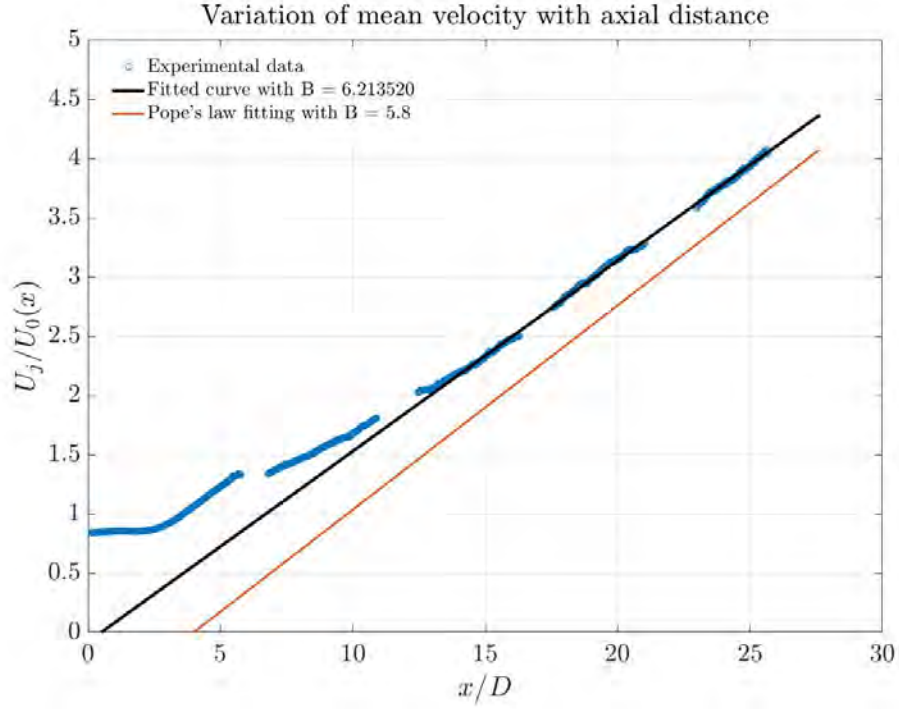


Figure 4.10: Variation of mean velocity with axial distance. One of the B values from Pope is also plotted to compare.

A similar outcome is seen in Fig. 4.10, where the variation becomes linear after some diameters. The obtained value for B is 6.21, relatively similar to the values from the different tests given in the book, which are 6.06, 5.9 and 5.8.

Notice that the values from the literature were fitted with data up to 100 diameters of axial distance, and thus if the tests in this setup were to be conducted for further distance, the coefficient B would be even closer. In any case, it is clear that the linear behaviour is achieved from around 15 diameters on, agreeing with the expected self-similarity behaviour of the velocity field seen previously.

Chapter 5

Temporal distribution of the project

Under this section, the time invested in the project will be accounted for, focusing mainly on how it was distributed along time. The work hours invested by the author were approximately 350 in a partial time regime over 9 months.

These work hours were distributed irregularly over the course of 9 months. This irregularity was due to the fact that many idles arised during the project development, which appeared whenever new elements had to be sent by the suppliers, or when the queue for the 3D printing machine was long.

Since the different tasks required communication between the tutors and the author, as well as decision making, they were usually overlapped, leading to the gantt chart presented below (Figure 5.1). It roughly measures the moments in which the different parts of the project were carried out. Each different segment of the project is presented with a different colour.

Since the facility was constructed from scratch, some design concepts would change to adapt to the different design needs that arised during the project's development. This was were the decision making lay, requiring the expertise of the tutors to choose the most appropriate ideas in each step.

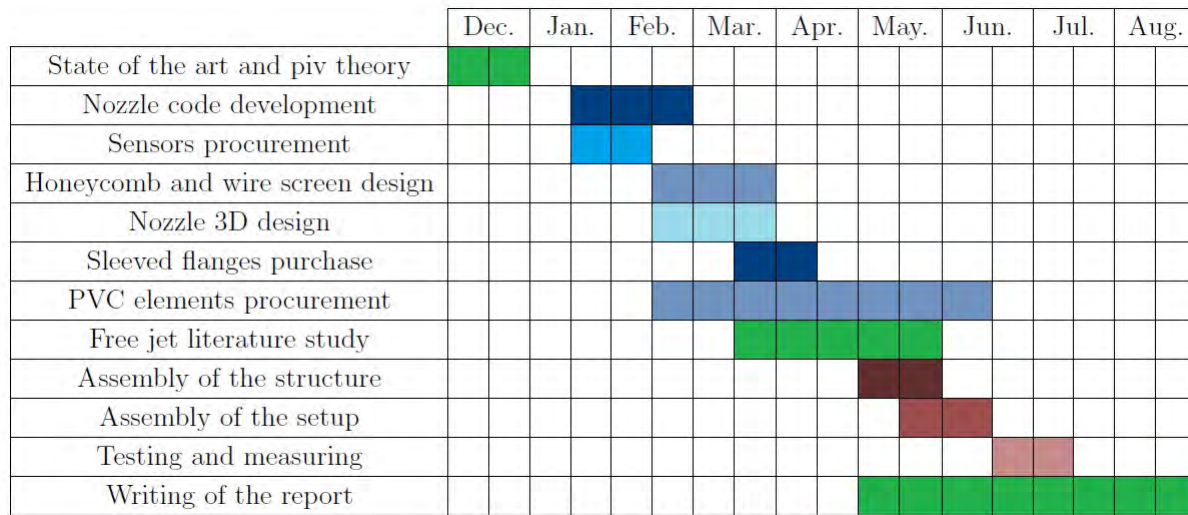


Figure 5.1: Gantt chart of the full project. In green, the theoretical work is presented. The work of procurement and design of the structure is marked with blue tones. The assembly of the structure is painted in brown colours.

Chapter 6

Costs calculation

As an experimental facility, it is interesting knowing how much could it cost to assembly one of them, in case a similar one was to be created in the future, either in this university or in other place.

The main costs come from the labour hours devoted by the author, as the materials used for the facility were usually the most cheap found. This line of acting could be held thanks to the requirements of the materials being low enough for regular elements to be suitable for their use here. If the pressures used were to be much higher (For example, for supersonic jet studies), the materials used would need to be stronger.

| | |
|---|--------|
| Black felt blanket | 74 € |
| Blind and sleeved flanges | 101 € |
| Hoses | 30 € |
| Ball valve | 13 € |
| Rest of PVC elements and extras (tubes, lids, etc.) | 39 € |
| Mosquito net | 1.5 € |
| 3D printings | 15 € |
| PIV equipment (Camera, laser and synchronizer) amortization | 1333 € |
| Labour hours | 3850 € |
| PC amortization | 52.5 € |
| Electricity | 11 € |
| Total | 5520 € |

Table 6.1: Project costs.

The PIV equipment is worth approximately 80 000 €, depreciated in five years. The time it was dedicated to this project was one month. For the PC, the value was 700 €, and it was depreciated over 2 years, being the used time 9 months with 20 % of dedication. The salary of the author was calculated assuming 1680€ per month, which translate to around 11€ per hour [19].

Some other considerations have to be made regarding the costs, however. The first one being that the salary calculated for the author is a net one, obtained from the source provided. The pertinent taxes should be taken into consideration for a more precise cost. Multiplying the salary times 1.4 is usually a good approximation with the current spanish legislation, which would make the "labour hours" cost 5390 € (Therefore raising the total cost to 7060 €).

Also regarding salaries is the fact that the author collaborated with both a doctorate and a technician from the university, and these costs should also be considered for a more exact estimation. However, since they did not regard the author, it is was not included in the calculations.

Lastly, the software used, i.e., Matlab and SolidEdge, require paid licences. Since the university provides licences to all of its students by using a campus license, it becomes difficult to calculate the licence price associated to the author, and hence it was not regarded here.

Chapter 7

Regulatory frame and future possibilities

7.1 Laboratory safety rules

The most direct regulations that this project was subject to were the security proceedings in the laboratory.

The potential hazards in the room, such as the enclosed seeding and mostly the light of the laser, which carried a level 4 (Being able to provoke injuries in the eye due to unwanted reflections, burn the skin or constitute a fire risk [8]) made it necessary to close both of the doors of the laboratory, even locking them from the inside to prevent any unexpected person stepping in. The laser also made necessary the use of protective goggles.

Using the pressure lines only when a supervisor was present, as well as not stepping too close to parts that have been recently assembled and not tested under pressure were some more of the rules followed.

7.2 Noise legislations

The main motivation for the studies that this project is intended to contribute to is the reduction of noise coming from civil aircraft. The strong legislations here, which impose

limits that are way too far from what technologies can achieve (The laws of Madrid, as an example, do not allow more than 35 dB of noise for residential areas [7]), force the airports to be usually far away from the urban nuclei, luckily in the surroundings if not further.

Furthermore, the noise maps that an airport project has to present are often costly and time-consuming, and in some cases they are not even enough, and controversies with the neighbours near these new airport arise. This makes the reduction of noise in aircraft an important socioeconomic issue that must not be overlooked.

7.3 Improvements

Once proven that the results are acceptable, the main changes in the setup could be used to improve the imaging process or to adapt the structure for tests with other conditions.

Firtsly, the big PVC cross may be used to give new inputs to the air, for instance, noise waves or increased temperature. Another possible adjustment would be changing the PVC materials with ones that can bear more pressure, although this solution does not seem to be needed in the near future.

A more resistant method of sticking the honeycomb and wire screens to the interior of the stagnation chamber would be necessary if the velocities of the experiment were to be increased. This may also need, as already mentioned in section 2.1, a redesign of the stagnation chamber, in order to adapt to the pressure losses and achieving higher pressures. This redesign may include making a longer stagnation chamber, in order to put more and smaller honeycombs or screen wires.

In case that more seeding is used, or the setup were to be transported to a chamber with less ventilation, a proper ventilation system would need to be designed and assembled to reduce hazards.

If the setup were to be assembled on a permanent place, several fixings to make sure that the camera shooting direction and the jet plane are exactly at 90° could be done. Furthermore, guide rails could be used to avoid the need of overlapping and recalibrating.

Chapter 8

Project conclusion

The main objective of this project was to procure, assembly and test a setup for a PIV study of free jets, and prove that it gave acceptable results. The different pieces were thoroughly explained and assembled in order to produce the best results possible, and leave room for changes in the setup for future experiments once given that it worked as it should.

The experiments were carried out with the author's collaboration in the tasks related with the laser and camera, and the results were treated to have measurements as clean as possible.

The experimental results were compared to the literature ones, finding reasonable agreements. The axial velocity and the turbulent magnitudes were not found self-similar after proper axial distances, but evidence that this special regime was being attained has been given.

It is then concluded that this setup functions correctly, and it can be adapted to perform other experiments that require the aid of PIV, with the correct adjustments and with the room for improvement mentioned in section 7.3.

Bibliography

- [1] Mendez M. A., Raiola M., Masullo A., Discetti S., Inairo A., and Theunissen R. and Buchlin J.M. POD-based background removal for particle image velocimetry. *Experimental Thermal and Fluid Science*, 80:181–192, 2018.
- [2] Jewel B. Barlow, William H. Rae, Jr., and Alan Pope. *Low-Speed Wind Tunnel Testing*. John Wiley & Sons INC., 1999.
- [3] B. J. Boersma, G. Brethouwer, and F.T.M. Nieuwstadt. A numerical investigation on the effect of the inflow conditions on the self-similar region of a round jet. *AIP Publishing, Physics of Fluids*, 10(4), 1998.
- [4] Giovanni Maria Carlomagno and Andrea Ianaro. Thermo-fluid-dynamics of submerged jets impinging at short nozzle-to-plate distance: A review. *Physics of Fluids*, 10(9), 2014.
- [5] John-Paul Clarke. The role of advanced air traffic management in reducing the impact of aircraft noise and enabling aviation growth. *Journal of Air Transport Management*, 9:161–165, 2003.
- [6] Stanley Corrsin. Investigation of flow in an axially symmetrical heated jet of air. *National Advisory Committee for Aeronautics*, 1943.
- [7] Consejería de medio ambiente y ordenación del territorio. [Webpage](#). Normativa de Ruidos y Vibraciones, 2004. Accessed: 08/09/2018.
- [8] Ministerio de Trabajo y Asuntos Sociales. [Webpage](#). NTP 261: Risk from laser use. Accessed: 08/09/2018.
- [9] Charlotta Eriksson, Mats Rosenlund, Görand Pershagen, Agneta Hilding, Claes-Höran Östenson, and Gösta Bluhm. Aircraft noise and incidence of hypertension. *Epidemiology*, 18(6), 2007.

-
- [10] Matteo Fabbri, Shanjuan Jiang, and Vijay K. Dhir. A Comparative Study of Cooling of High Power Density Eletronics Using Sprays and Microjets. *Journal of Heat Transfer*, 127, 2005.
- [11] W. K. George. The self-preservation of turbulent flows and its relation to initial conditions and coherent structures. In *Advances in turbulence*, pages 39–73. Springer, Berlin, 1989.
- [12] E. Gutmark and I. Wygnanski. The planar turbulent jet. *J. Fluid Mech.*, 73(3):465–495, 1976.
- [13] M.M. Haines, S.A. Stansfeld, R.F.S. Job, B. Berglund, and J.Head. Chronic aircraft noise exposure, stress responses, mental health and cognitive performance in school children. *Psychological Medicine*, 31(2):265–277, 2001.
- [14] B. Han and R. J. Goldstein. Jet-Impingement Heat Transfer in Gas Turbine Systems. *Heat Transfer Laboratory*, 2006.
- [15] Gunnar Heskestad. Hot-Wire Measurements in a Plane Turbulent Jet. *Journal of Applied Mechanics*, 9(2), 1965.
- [16] M. S. Howe. Contributions to the theory of aerodynamic sound, with applicatoin to excess jet noise and the theory of the flute. *J. Fluid Mech.*, 71(4):625–673, 1975.
- [17] [Webpage](#). Horizon 2020: Topic: Reducing aviation noise. Accessed: 28/08/2018.
- [18] [Webpage](#). Horizon 2020: Smart, Green and Integrated Transport. Accessed: 28/08/2018.
- [19] [Webpage](#). Boletín Oficial del Estado, Miércoles 18 de enero de 2017. III. Otras disposiciones.
- [20] Glenn Research Center. [Webpage](#). Making future commercial aircraft quieter. Glenn effort will reduce engine noise. Accessed: 21/09/2018.
- [21] [Webpage](#). Report to the European Parliament on the socioeconomic impact of Clean Sky. Accessed: 28/08/2018.
- [22] Dennis L. Huff. Noise Reduction Technologies for Turbofan Engines. *National Aeronautics and Space Administration*, 2007.
- [23] A. K. M. Fazle Hussain. Coherent structures-reality and myth. *Phys. Fluids, American Institute of Physics*, 26, 1983.

-
- [24] A. K. M. Fazle Hussain. Coherent structures and turbulence. *J. Fluid Mech.*, 173:303–356, 1986.
- [25] Hussein J. Hussein, Steven P. Capp, and William K. George. Velocity measurements in a high-reynolds-number, momentum-conserving, axisymmetric, turbulent jet. *Cambridge university Press, J. Fluid Mech.*, 258:31–75, 1994.
- [26] M. J. Lighthill. On sound generated aerodynamically i. general theory. *Proceedings of the Royal Society of London A: Mathematical, Physical and Engineering Sciences*, 211(1107):564–587, 1952.
- [27] John N. B. Livingood and Peter Hrycak. Coherent structures and turbulence. *NASA Technical Memorandum*, 1973.
- [28] M.N. Mikhail and W.J. Rainbird. Optimum design of wind tunnel contractions. *Dilworth, Secord, Meagher and Associates Limited*, 1978.
- [29] Stephen Morrell, Richard Taylor, and David Lyle. A review of health effects on aircraft noise. *Australian and New Zealand Journal of Public Health*, 21(2), 1997.
- [30] N. R. Panchapakesan and J. L. Lumley. Turbulence measurements in axisymmetric jets of air and helium. Part 1. Air jet. *Cambridge University Press, Fluid Mech.*, 246:197–223, 1993.
- [31] Stephen B. Pope. *Turbulent Flows*. Cambridge University Press, 2000.
- [32] Czeslaw O. Popiel and Olev Trass. Visualization of a free and impinging round jet. *Experimental Thermal and Fluid Science*, 4:253–264, 1991.
- [33] Discetti S. and Coletti F. Volumetric velocimetry for fluid flows. *Measurement Science and Technology*, 29(4), 2018.
- [34] A. Sarkar, N. Nitin, M. V. Karwe, and R.P. Singh. Fluid Flow and Heat Transfer in Air Jet Impingement in Food Processing. *Journal of Food Science*, 69(4), 2006.
- [35] Fulvio Scarano. Tomographic PIV: principles and practice. *Meas. Sci. Technol.*, 2013.
- [36] Fulvio Scarano and Jerry Westerweel. Part i: Fundamentals of Particle Image Velocimetry. *Course notes for Advanced Image Velocimetry*, 2008.
- [37] Barton L. Smith and Ari Glezer. The formation and evolution of synthetic jets. *Experimental Thermal and Fluid Science*, 58:15–35, 1998.

-
- [38] Tarnopolsky, A., Barker, S. M., Wiggins, R. D., McLean, and E. K. The effect of aircraft noise on the mental health of a community sample: a pilot study. *Psychological Medicine*, 8(2):219–233, 1978.
- [39] The university of Utah. [Webpage](#). Lenght and time scales in turbulent flows. Accessed: 23/09/2018.
- [40] Daniele Violato. 3D flow organization and dynamics in subsonic jets. Aeroacoustic source analysis by tomographic PIV. 2013.
- [41] Nannan Wu, Yasuhiko Sakai, Kouji Nagata, Yasumasa Ito, Osamu Terashima, and Toshiyuki Hayase. Influence of Reynolds number on coherent structure, flow transition, and evolution of the plane jet. *Journal of Fluid Science and Technology*, 2013.